Alpha and high gamma phase amplitude coupling during motor imagery and weighted cross-frequency coupling to extract discriminative cross-frequency patterns

Daeun Gwon [a], Minkyu Ahn [a,b,*]

[a] Department of Information and Communication Engineering, Handong Global University, 37554 South Korea
[b] School of Computer Science and Electrical Engineering, Handong Global University, 37554 South Korea

A B S T R A C T

Motor imagery modulates specific neural oscillations like actual movement does. Representatively, suppression of the alpha power (e.g., event-related desynchronization [ERD]) is the typical pattern of motor imagery in the motor cortex. However, in addition to this amplitude-based feature, the coupling across frequencies includes important information about the brain functions and the existence of such complex information has been reported in various invasive studies. Yet, the interaction across multiple frequencies during motor imagery processing is still unclear and has not been widely studied, particularly concerning the non-invasive signals. In this study, we provide empirical evidence of the comodulation between the phase of alpha rhythm and the amplitude of high gamma rhythm during the motor imagery process. We used electroencephalography (EEG) in our investigation during the imagination of left- or right-hand movement recorded from 52 healthy subjects, and quantified the ERD of alpha and phase-amplitude coupling (PAC) which is a relative change of modulation index to the base line period (before the cue). As a result, we found that the coupling between the phase of alpha (8–12 Hz) and the amplitude of high gamma (70–120 Hz) and this PAC decreases during motor imagery and then rebounds to the baseline like alpha ERD ($r = 0.29$ to 0.42). This correlation between PAC and ERD was particularly stronger in the ipsilateral area. In addition, trials that demonstrated higher alpha power during the ready period (before the cue) showed a larger ERD during motor imagery and similarly, trials with higher modulation index during the ready period yielded a greater decrease in PAC during imagery. In the classification analysis, we found that the effective phase frequency that showed better decoding accuracy in left and right-hand imagery, varied across subjects. Motivated by result, we proposed a weighted cross-frequency coupling (WCFC) method that extracts the maximal discriminative feature by combining band power and CFC. In the evaluation, WCFC with only two electrodes yielded a performance comparable to the conventional algorithm with 64 electrodes in classifying left and right-hand motor imagery. These results indicate that the phase-amplitude frequency plays an important role in motor imagery, and that optimizing this frequency ranges is crucial for extracting information features to decode the motor imagery types.

1. Introduction

Electrophysiological oscillations in neural populations are promising measures with which to investigate brain functions. Typically, these oscillations are categorized into several frequency bands such as delta (Knyazev, 2012), theta (Klimesch, 1999), alpha (Foster et al., 2017), beta (Baumeister et al., 2008), gamma wave (Lutz et al., 2004). Recently, amplitude (or power) at a specific frequency or functional connectivity (e.g., correlation, coherence, phase locking value) between two locations, are investigated to study brain functions.

However, over the past decades, connectivity or coupling across different frequency bands has been introduced in neuroscience studies. Indeed, some neural processing may rely on a nonlinear mechanism that may not be observable at a specific frequency, but may be quantified by coupling across frequencies. This cross-frequency coupling (CFC) has been given attention in investigating complex brain functioning. Recent empirical evidence has suggested that interactions across different frequency bands are present in animal and human brains (Axmacher et al., 2010; López-Azcárate et al., 2013; Whittingstall and Logothetis, 2009). This provides us with new insight and the need to explore a broader space in brain research. An oscillatory signal consists largely of two components (e.g., amplitude and phase), and thus, several CFC metrics across frequencies can be calculated (e.g., Amplitude to Amplitude, Phase to Phase and Phase to Amplitude). Among them, Phase-Amplitude

Coupling (PAC) is the measure studied best that reflects the coupling between the phase of low frequency and the amplitude of high frequency (Canolty et al., 2006; Canolty and Knight, 2010; Meij et al., 2012; Penny et al., 2008; Tort et al., 2010, 2008; van Wijk et al., 2015; Voytek et al., 2013).

To data, PAC has been used in studies of various brain functions, and the results have revealed that it is a promising measure. A human decision-making study (Cohen et al., 2008) reported that PAC increased in the medial frontal cortex during a competitive decision-making game. Specifically, the coupling of the alpha phase and beta power increased significantly when defeated subjects made decisions. The coupling of the alpha/theta phase and gamma amplitude has also been shown to increase in the visual cortex during visual stimulation (Voytek et al., 2010). Further, the burst gamma locked the phase of alpha wave in the default network of a resting state (Bahramisharif et al., 2013).

Meanwhile, there has been renewed interest as well in the connection between motor function and CFCs. A complex neuronal process mediates motor function and entails increase or decrease in amplitude at specific frequency bands. Decreased alpha and beta, referred to as event-related desynchronization (ERD), and increased gamma are the typical patterns when executing movement (Pfurtscheller and Lopes da Silva, 1999), and this is the key feature in motor imagery brain-computer interface, as such amplitude changes arise while observing movement (Yanagisawa et al., 2012) and during imagination (Pfurtscheller and Neuper, 1997).

However, recent studies have also found the important engagement of phase information in the neuronal processing of movement. Indeed, low-frequency components seem to encode various movement features such as position, velocity and acceleration (Combrisson et al., 2017; De Lange et al., 2008; Hammer et al., 2016, 2013; Jerbi et al., 2011; Milekovic et al., 2012; Miller et al., 2012; Waldert et al., 2009). Further, empirical evidence has shown the presence of cross-frequency coupling (e.g., PAC) in motor function, in which frontal beta and posterior gamma coupling were observed while imagining movement (De Lange et al., 2008). Excessive coupling of beta and gamma in the primary motor cortex (M1) was reported in Parkinson's disease patients who suffer from abnormal movement (Bichsel et al., 2018; Hemptinne et al., 2013; Jenkinson et al., 2013). In one study that investigated the functional role of PAC (Combrisson et al., 2017), strong PAC between alpha and gamma during motor planning was observed in the anterior cingulate cortex and premotor brain area when performing a goal-directed motor behavior on its planning and execution. Summarizing these results, phase and PAC information are present during movement and it seems clear that understanding their functional role is important to study motor function. However, despite interesting findings and advances, PAC during the motor imagery process, particularly the presence of PAC while imagining movement and PAC lateralization in left- and right-hand imagination has not been investigated fully.

In this study, we demonstrated that alpha and gamma PAC also presents during the motor imagery process, particularly using noninvasive electroencephalography (EEG). This PAC during motor imagery is also compared with alpha ERD. Further, the laterality of PAC in left/right- motor imagery was investigated to determine the feasibility of using in brain-computer interface. We also proposed a novel machine learning method to extract cross-frequency coupling that can be highly effective in classifying two conditions.

2. Materials and methods

2.1. Data and preprocessing

For this study, we used two publicly available EEG datasets recorded during conventional motor imagery experiment. The descriptions of the datasets are as follows.

Dataset 1. Fifty-two healthy subjects participated in this experiment and conducted 100 or 120 trials of left- or right-hand motor imagery (Cho et al., 2017). In each trial, a fixation cross was displayed for 2 s, and then an instructional cue that show the direction of imagination (left or right) was presented for 3 s. During this period, subjects conducted motor imagery while EEG was acquired using a 64-channel EEG amplifier according to the 10–20 international system and sampled at 512 Hz.

Dataset 2. This dataset, referred to as BCI Competition IV 2b, included EEG data from nine healthy subjects. Signals were recorded from three locations (C3, Cz and C4) at a 250 Hz sampling rate (Leeb et al., 2007). Each dataset consisted of training (TrainSet) and testing (TestSet) sessions. In two training sessions, a directional arrow was presented for 4.5 s. as an instructional cue after a 3 s. fixation cross. The subjects conducted motor imagery during the presentation of the directional arrow, and received no feedback of the motor imagery. In the following testing sessions, a colored smiley was presented for 4 s. after a 3 s. grey smiley to instruct the subjects to perform either left- or right-hand motor imagery. During this period, the color smiley moved toward the classified direction to give the subjects feedback. Each subject conducted 120 trials and 160 trials during the training and testing sessions, respectively.

2.2. ERD calculation

To determine the ERD pattern, the alpha (8–12 Hz) rhythm was isolated by frequency filtering, and the power at each window was converted into percentage power by defining the power within a reference period (-1,800 ms to 0 ms). The window size was set to 1,800 ms and the temporal ERD series was obtained by shifting the window by 100 ms. This process was conducted on each motor imagery trial. Specifically, for the ith window in the jth epoch, $ERD_{i,j}$ was calculated from the magnitude squared power, $P_{i,j}$, within the ith window and the epoch-averaged power $P_r = \langle P_{r,j} \rangle_j$ during a reference period r (-1,800 ms to 0 ms) with the following equation:

$$ERD_{i,j}(\%) = \left(\frac{P_{i,j} - P_r}{P_r} \right) \times 100\ (\%).$$

2.3. PAC calculation

To estimate PAC, we used the Modulation Index, MI (Tort et al., 2008), which measures cross-frequency coupling based on Shannon entropy and Kullback-Leibler (KL) divergence. The MI is reported to be robust to noisy and short epochs (Hülsemann et al., 2019). Given two filtered signals, $x_A \in R^{1 \times T}$ and $x_p \in R^{1 \times T}$, the time series, ϕ_p, of the phases of x_p, and the time series, E_A, of the envelope amplitude of x_A can be calculated from the Hilbert transform. Then, the MI from x_p to x_A can be computed based on the following procedure.

First, all possible phases (0 to 360°) are binned into N bins; usually, 18 is suggested (Tort et al., 2008) and we also used this number for N. Then, the mean amplitude, p_j, of the amplitude frequency in each phase bin j of the phase frequency is computed and normalized by the total mean amplitude across the N phase bins. We denote $\langle E_A \rangle_{\phi_p}(j)$ as the mean E_A value at phase bin j:

$$p_j = \frac{<E_A>_{\phi_p}(j)}{\sum_{k=1}^{N} <E_A>_{\phi_p}(k)}$$

Second, Shannon entropy (H) is calculated by the following formula $H(p) = -\sum_{j=1}^{N} p_j \log(p_j)$, in which p is the vector of amplitudes per phase bin. Finally, MI is calculated by Kullback-Leibler divergence, $D_{KL}(U, p)$, which measures the disparity in two distributions, and normalized with the formula:

$$MI = \frac{D_{KL}(U, p)}{\log(N)} = \frac{\log(N) - H(p)}{\log(N)}$$

where U is the uniform distribution that yields the maximum possible entropy $\log(N)$. Thus, a larger MI indicates that p is far from U by Kullback-Leibler divergence.

In general, minimizing the distortion in the phase information in each signal to estimate the MI accurately is important. To do this, we applied empirical mode decomposition (EMD) that is suitable for processing time series data that are non-stationary and non-linear, and well disassembles residuals from signal (Huang et al., 1998). Because of this advantage, EMD was used in various studies (Al-Subari et al., 2015; Pittman-Polletta et al., 2014; Tsai et al., 2019; Zhang et al., 2008). This method decomposes a given time series into a series of component called intrinsic mode functions (IMFs) and a residual component. In this study, we conducted baseline correction by removing the residual component estimated by EMD.

Then band-pass filtering was performed to isolate alpha (phase frequency: 8–13 Hz) and high gamma (amplitude frequency: 40–120 Hz in a 20 Hz bandwidth and 10 Hz step size). The first and last 100ms of the signals were removed to prevent introducing signal distortion attributable to frequency filtering. The instantaneous phase and amplitude components were extracted by the Hilbert transform.

Thereafter, we obtained the MI series in each amplitude frequency by shifting the fixed size window by 100 ms, as shown in Fig. 2D. Here, the size of the window was set to 1,800 ms. Then, PAC, which is the MI value relative to MI during a reference period, was computed with the following formula:

$$PAC_{i,j}(\%) = \left(\frac{MI_{i,j} - MI_r}{MI_r} \right) \times 100 \ (\%)$$

where $MI_{i,j}$ is the modulation index of the ith time window in the jth epoch and $MI_r = \langle MI_{r,j} \rangle_j$ is the average MI across epochs during a reference period r (-1,800 ms to 0 ms). The resultant PAC facilitates investigation of temporal behavior of MI compared to the reference before the motor imagery period.

2.4. ERD and PAC analysis

In this study, we focused first on the alpha rhythm, which is associated with executing and imagining movement. As alpha ERD arises during the motor imagery process, our goal was to determine whether a similar change also presents in alpha-PAC. Because of the lack of knowledge of amplitude frequency, we examined the temporal changes in PAC initially, as shown in Fig. 2D and Fig. 4A, and manually chose 70–120 Hz which covers a broad band of upper gamma rhythms. Then, alpha-PAC during motor imagery was analyzed on the C3 and C4 channels for left/right hand motor imagery. To minimize any possible bias from outliers (Schwertman and de Silva, 2007), we removed some epoch by using interquartile range (IQR) which is frequently used in EEG analysis, machine learning and deep learning (Ermiş et al., 2020; Qiu et al., 2020; Stevenson et al., 2015). With the third quartile Q3 (75%) and the first quartile Q1 (25%) of the overall distribution, the IQR was set as Q3 – Q1 and we removed epochs that do not fall into the range between Q1 + 2 × IQR and Q3 + 2 × IQR. Approximately 8.2% of the data was removed, and those setting were used throughout the study, except for accuracy calculation of classification.

Next, we compared the temporal patterns of alpha ERD and alpha-high gamma PAC using the Pearson's Correlation Coefficient to see the similarity. Epoch-wise correlation coefficients were computed using the average per subject. These individual's correlation coefficients were collected, and a histogram was constructed. The skewness of the histogram was calculated to check the major direction of the correlation coefficients distribution.

We also analyzed the association between two states (*T0*: ready block and *T2*: imagery block) by using Spearman's correlation analysis. The correlation coefficient was calculated between the alpha power or the modulation index at ready block (*T0*) and the relative changes of alpha power (measured by ERD) and of MI (measured by PAC) at imagery block (*T2*), and statistical significance was obtained from randomization of pairs. For solid results, we identified outliers which are beyond 95% of each distribution based on Mahalanobis distance (De Maesschalck et al.,

2000), which is a useful method for outlier removal in the multivariate distribution (Kim, 2000). Then recalculated the correlation coefficient and the significance of the result only with the data after outlier removal.

In the analysis of left- versus right-hand imagery, PAC values were estimated for each epoch. As we could not see a significant difference between left and right imagery in alpha-high gamma PAC, we divided the broad frequency band (4 – 40 Hz) into five phase frequencies (*F1*: 4–8 Hz, *F2*: 8–12 Hz, *F3*: 12–20 Hz, *F4*: 20–28 Hz and *F5*: 28–40 Hz), but fixed interval of amplitude frequency to 70–120 Hz. The percent value of the MI was calculated from the motor imagery period, which was 600 ms to 2,400 ms, as in the other analysis. Then statistical tests were conducted for each subject to determine whether the PAC in left/right-hand imagery differed significantly. To evaluate PAC for left/right-hand imagery classification further, we introduced a machine learning algorithm and a 10 × 10-fold cross-validation technique. Epochs were divided into 10 groups, and Linear Discriminant Analysis (LDA) model was constructed with training samples in nine groups and tested with testing samples in one group. Then the final decoding accuracy (DA) was obtained for each subject. This was conducted repeatedly for each phase frequency.

2.5. Statistical test

We conducted the Student's t-test or one-way analysis of variance (ANOVA) to test the statistical significance among the conditions. For classification analysis of dataset 2, the Wilcoxon signed-rank test was used since there are only nine data. For multiple comparisons, the False discovery rate (FDR) correction (Benjamini and Hochberg, 1995; Genovese et al., 2002) was applied. Basically, the significance level was set to $p < 0.05$, and q was set to 0.05 for the FDR correction.

Estimating phase amplitude coupling is reported as being sensitive to the signal-to-noise ratio and waveform shape that might introduce spurious coupling. This is why relevant studies recommend conducting surrogate analysis to estimate statistical chance (Aru et al., 2015; Genovese et al., 2002; Kramer et al., 2008; Lozano-Soldevilla et al., 2016). Therefore, to confirm the statistical significance of MI results, comparing them with surrogate data is highly recommended. In this study, we also generated surrogate data ($N = 200$) by shuffling epochs, thus two time series (phase and amplitude) were randomly paired across epochs. This is a conservative approach that minimizes distortion of phase and amplitude dynamics that, consequently, can reduce the number of false positives as suggested in the related studies (Aru et al., 2015; Canolty et al., 2006).

For classification analysis, we also generated the statistical chance accuracy by shuffling the true labels of epochs. This shuffling was done before splitting training and testing data sets to generate the fully randomized chance level. In each shuffling we estimated a classification accuracy, and the final statistical chance level was obtained by averaging the estimates from 100 iterations. Then this chance accuracy was compared with the actual classification accuracy to check the statistical significance.

2.6. Weighted cross-frequency coupling (WCFC)

Frequency ranges that discriminate between the signals of two given conditions (e.g., left- and right-hand motor imagery) maximally, may vary across sessions or subjects. This means that subject specific phase and amplitude frequencies need to be chosen to achieve reasonable classification performance (see Fig. 7). However, conventional phase-amplitude coupling methods, including the MI, produce only the coupling between two specific frequencies. This means that identifying proper frequency components or classifiable MIs requires repeated phase-amplitude coupling estimation and evaluations to search for the optimal phases and amplitude frequencies. A mathematical optimization of phase-amplitude coupling that are designed for the classification
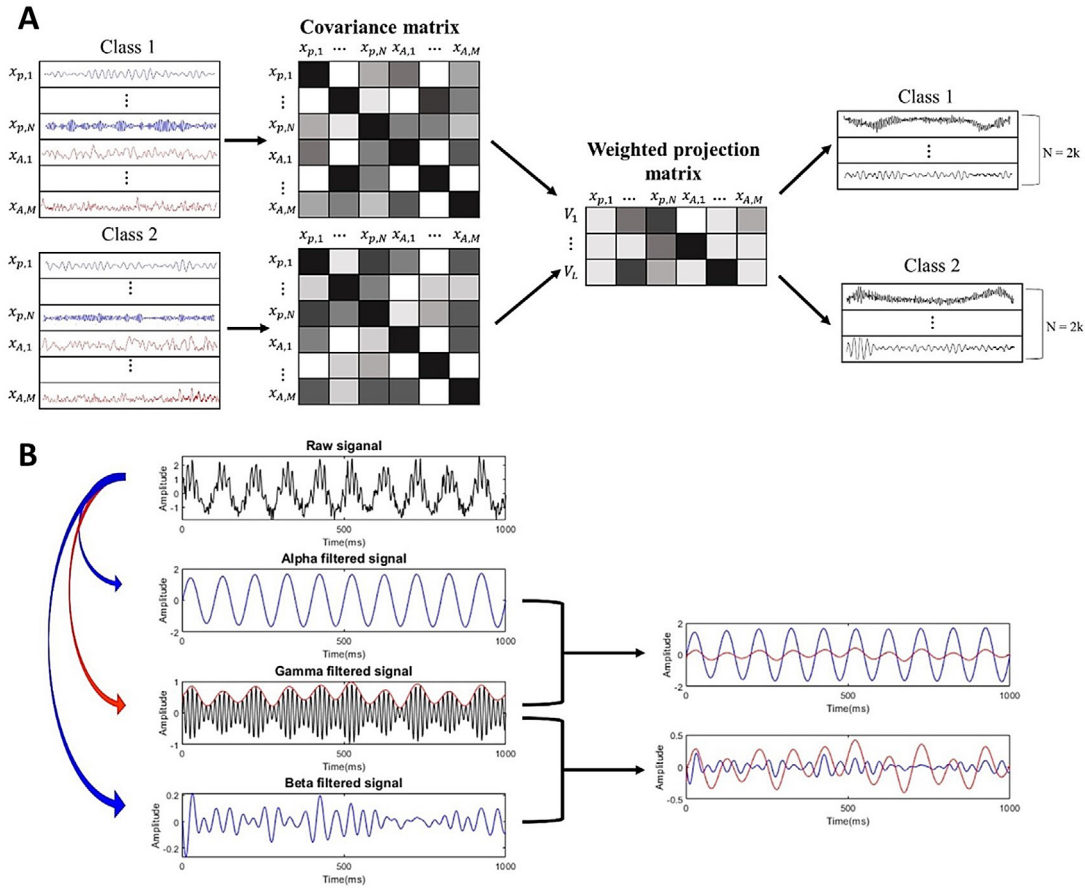
Fig 1. Schematic representation of the WCFC analysis principle (A) Illustration of calculating features using the weighted projection matrix from two different conditions' filtered signals. (B) Example of the principle using a covariance matrix among decomposed signals. Three frequency signals (alpha, beta and gamma) are presented. A correlation analysis revealed that the alpha rhythm is correlated highly with the envelop (solid red line) of gamma ($r = 0.8954$, $p = 2.1971e\text{-}181$), while the beta rhythm is not ($r = 0.1823$, $p = 3.3327e\text{-}05$). Obviously, phase amplitude coupling calculated by MI is higher in alpha-gamma (MI = 0.0158) than in beta-gamma (MI = 6.5678e-04).

of conditions, would be one potential way. However, incorporating a phase-amplitude coupling algorithm into such a classification problem is not easy due to the complex process of phase-amplitude coupling algorithms. Thus, this approach requires the phase-amplitude coupling estimate that is much more computationally feasible and implementable. In this section, we introduce a novel feature extraction method that is advantageous in addressing various CFC features. Especially, we will use correlation-based CFC for the classification problem.

The proposed method extracts weighted CFC features that discriminate two given conditions maximally. We do not use the MI to estimate the phase-amplitude coupling, but correlation-based estimates. Given the basic notion of MI that low frequency modulates high frequency, a simple correlation between the low frequency signal and the high frequency envelop will also provide an estimate of phase-amplitude coupling (Bruns and Eckhorn, 2004; Canolty et al., 2006; Maris et al., 2011; Tort et al., 2010). Fig. 1B briefly describes this principle. The alpha rhythm was correlated positively with the envelop of gamma ($r = 0.8954$, MI = 0.0158), while beta showed a poor correlation ($r = 0.1823$, MI = 6.5678e-04). Accordingly, the phase-amplitude coupling is much higher in alpha and gamma than in beta and gamma. With this basic idea, we can construct an optimization problem and obtain a weighted filter for a two-class problem. The procedure for the proposed method is shown in Fig. 1.

Let $x \in R^{1 \times T}$ be a segment of the EEG signal that is an epoch of motor imagery; T is the number of time samples in the epoch. This x can be represented by the composition of various sub frequency components $x_f \in R^{1 \times T}$ with different frequencies $f = 1, 2, \ldots, F$. Among

these sub frequency signals, the signal of the low frequency matrix, is equivalent to the phase frequency in the previous method, $X_P = (x_{P,1}^T, \ldots, x_{P,m}^T, \ldots, x_{P,M}^T)^T$, and an amplitude frequency matrix, $X_A = (x_{A,1}^T, \ldots, x_{A,m}^T, \ldots, x_{A,N}^T)^T$, can be created by stacking the M and N frequency components, respectively. These were filtered using a two-way least-squares FIR filter (eegfilt.m function in EEGLAB) to minimize damaging the phase without the windowing. Here, $x_{P,m}$ and $x_{A,n}$ are chosen from the set $\{x_f\}_{f=1}^F$ and T denotes the transposition of a given vector or matrix. By applying the Hilbert transform and absolute operation to X_A, envelope matrix E_A can be obtained. For simplicity, let us define $L = M + N$; then a multi-frequency matrix $Z \in R^{L \times T}$ can be obtained:

$$Z = \begin{pmatrix} X_P \\ E_A \end{pmatrix}. \tag{1}$$

To scale each frequency component in Z, z-scoring on each row is conducted using the sample mean and standard deviation calculated from the signal during the ready state (before the cue). This operation creates a normalized matrix $\bar{Z}$ that ideally follows $N(0, 1)$. Finally, we can obtain estimates of the CFC features by calculating a covariance matrix $C \in R^{L \times L}$ in which an element $c_{a,b}$ in the a-th row and b-th column in C represents the correlation between the $\bar{z}_a$ and $\bar{z}_b$ frequency components in $\bar{Z}$. We refer to this C as the CFC matrix.

Now, we find a weight vector that projects the multi-frequency matrix $\bar{Z}$ for a two-class problem. Given class label $i \in \{1, 2\}$, let $\Sigma_1 \in R^{N \times N}$ and $\Sigma_2 \in R^{N \times N}$ be CFC matrices in two conditions. They can be calculated as $\Sigma_i = \langle C_i(e) \rangle$, in which $C_i(e)$ is the CFC matrix of an epoch e and

$\langle \cdot \rangle$ denotes the average across epochs. A weight vector w should enhance the difference in the CFC features between two conditions. With this goal, an objective function $J(w)$ for condition 1 can be written as

$$J(w) = \frac{w^{\mathrm{T}} \Sigma_1 w}{w^{\mathrm{T}} \{\Sigma_1 + \Sigma_2\} w}. \tag{2}$$

This Rayleigh quotient can be rewritten as an optimization problem with a constraint,

$$\max_w w^{\mathrm{T}} \Sigma_1 w, \text{ Subject to } w^{\mathrm{T}} \{\Sigma_1 + \Sigma_2\} w = 1 \tag{3}$$

This problem can be solved using Lagrange multipliers and the solution $\hat{w} \in \mathrm{R}^{L \times 1}$ satisfies $\Sigma_1 \hat{w} = \lambda(\Sigma_1 + \Sigma_2)\hat{w}$, that is a generalized eigenvalue problem. For the eigen values of both classes, we can easily drive $\lambda_1 + \lambda_2 = 1$ from the constraint in Eq. (3). By assuming that L eigenvectors $\{\hat{w}_j\}_{j=1}^{L}$ are sorted on eigen values $\hat{\lambda}_1 > \hat{\lambda}_2, \ldots, > \hat{\lambda}_L > 0$, then $\hat{w}_1$ with the largest eigen value maximizes the variance (or CFC) of class 1, while it minimizes the common variance. In addition, the eigenvector $\hat{w}_j$ with a small $\hat{\lambda}_j$ will maximize the variance of class 2 because $\lambda_2 = 1 - \lambda_1$. Thus, the first and last eigen vectors have the opposite effect on the given CFC matrix C. Here we compute the scaling factor $a_j > 0$ from each eigen value $\hat{\lambda}_j$ by $a_j = |\hat{\lambda}_j - \langle \hat{\lambda}_k \rangle_k|$, in which $\langle \hat{\lambda}_k \rangle_k$ is the average of the eigen-values. By applying each $\hat{w}_j$ and scaling factor a_j to a given CFC matrix C, the weighted CFC $s_j \in \mathrm{R}^{1 \times 1}$ can be obtained as $s_j = a_j \hat{w}_j^{\mathrm{T}} C \hat{w}_j$ which will be larger for class 1 if $j = 1$. Here, we introduced a_j, the magnitude of the centered $\hat{\lambda}_j$ (the variance of $\hat{w}_j^{\mathrm{T}} C \hat{w}_j$), to weight each feature. If the C is Σ_1, then $s_j = a_j \hat{\lambda}_j$. Finally, the weighted projection vector v_j can be obtained by combining the eigen vector $\hat{w}_j$ and value $\hat{\lambda}_j$ as $v_j = \sqrt{a_j} \hat{w}_j$, consequently $s_j = v_j^{\mathrm{T}} C v_j$.

In a practical classification setting, multiple weight vectors are used. Thus, we target eigen-vectors and the corresponding Eigen values are selected from both ends of the solution set $\{\hat{w}_j\}_{j=1}^{L}$, and then the weighted projection matrix $V \in \mathrm{R}^{L \times 2k}$ can be constructed as $V = [v_1, \cdots, v_k, v_{L-k+1}, \cdots, v_L]$.

This weighted projection matrix can be applied directly to the CFC matrix $C(e)$ of given epoch e to generate feature vector $d(e) \in \mathrm{R}^{2k \times 1}$,

$$d(e) = diag(V^T C(e) V). \tag{4}$$

Where $diag(\cdot)$ extracts the diagonal of a given matrix. Please note that a classifier would fail to capture the difference between two classes if the k is too small, while it would overfit if k too large (Blankertz et al., 2008). Hence, in this study, we used $k = 4$.

2.7. Performance evaluation

WCFC is designed to find a weighted projection vector that maximizes the discriminability between two classes. This ability was tested with two motor imagery datasets, each of which was processed as follows.

The time interval for dataset 1 were set to -1,800–0 ms for the ready state and 500–3,500 ms for the motor imagery state respectively. Based on the intervals, EEG signals were segmented to produce epochs, and then normalized. Phase frequencies were chosen from the interval 4–40 Hz with a 4 Hz bandwidth and a 2 Hz moving step. For amplitude frequencies, relatively larger bandwidth (20 Hz) and moving step (10 Hz) were used to select frequencies from 40–140 Hz. This yielded 17 phase frequencies and 9 amplitude frequencies.

For dataset 2, the EEG was segmented into motor imagery epochs (500–4000 ms) and normalized using pre-cue EEG (-2000–0 ms). The phase frequencies were the same as in dataset 1, but a smaller number of amplitude frequencies was used, as the frequency available in this dataset is 125 Hz because of the Nyquist rule and 250 Hz sampling rate. Thus, amplitude frequencies were chosen from a shorter interval, 40–90 Hz, than in dataset 1, but with the same bandwidth (20 Hz) and moving step (10 Hz). Finally, 17 phase frequencies and 4 amplitude frequencies were used for WCFC.

We used 4 for k, which determines the number of weighted projection vectors, and the regularized linear discriminant analysis (LDA) (Guo et al., 2007) was employed for classification. The classification accuracy of WCFC combined with LDA was estimated from a 10×10-fold cross-validation per subject for dataset 1. However, for dataset 2, a classifier constructed based on TrainSet was evaluated with TestSet to compare the competition's results. In both datasets, a weighted projection matrix was constructed from left and right CFC matrices of training data, and then were applied back to the individual epochs of the training data to generate feature sets. An LDA classifier was constructed from the feature sets. Finally, the weighted projection matrix and the classifier were applied to testing data for performance estimation. Thus, no samples from the testing data were involved in obtaining parameters for feature transformer and classifier. The WCFC was tested with the C3 or C4 channels. We also attempted to combine feature vectors from both channels. When two channels were used, the feature vectors from both were simply concatenated and evaluated. Thus, WCFC1 denotes when a single electrode was used while WCFC2 represents the feature combination from the two electrodes.

For comparison, we evaluated different features. Two types of PSDs were estimated from different frequency intervals. With a nonoverlapping window and 8Hz bandwidth, 12 PSD features were computed from frequency interval 4 – 100Hz (e.g., 4–12 Hz, 12–20 Hz, 20–28 Hz …). We denote this as BrPSD (broad band PSD) which typically covers both phase and amplitude frequencies. NrPSD (narrow band PSD) was estimated from a shorter interval 4–40 Hz that includes only theta to gamma rhythms. With a 4 Hz bandwidth, and nonoverlapping window, 9 PSD features were obtained for NrPSD (e.g., 4–8 Hz, 8–12 Hz, 12–16 Hz …). Band-specific powers were calculated by Fourier transform (pspectum.m function in Signal Processing toolbox in MATLAB) for both BrPSD and NrPSD.

We also used a Common Spatial Pattern (CSP), which is known to demonstrate good performance (Blankertz et al., 2008), in classifying motor imagery EEG. CSP was used in the original paper (Cho et al., 2017) that published dataset 1 and was widely employed in various motor imagery studies (Fu et al., 2020; Mahmood et al., 2017; Shang-Lin Wu et al., 2013; Thomas et al., 2009; Wang et al., 2005). This method finds a spatial filter that maximizes the variance of class 1 and minimizes the variance of class 2. As it is designed to find a spatial filter, several electrodes are required. We applied CSP to dataset 1 as only signals from 64 electrodes were available in this dataset. As in conventional processing for motor imagery and CSP, signals were filtered to isolate alpha and beta waves (8–30 Hz) and 8 spatial filters were estimated to yield the 8 most discriminative features. For both PSD and CSP features, LDA was employed as a classifier.

In summary, classification accuracies with the LDA classifier were estimated and compared across different feature extraction methods (WCFC1, WCFC2, BrPSD, NrPSD and CSP).

3. Results

3.1. Alpha-high gamma PAC decreases during motor imagery

Fig. 2 presents an exemplary trial at C3 during left-hand motor imagery from one subject in dataset 1. The alpha decrease during motor imagery is observable, as shown in the raw, alpha and gamma oscillations (Fig. 2B). By quantifying the power, such a decrease is very clear in the time series of ERD (Fig. 2D). As the alpha ERD fluctuates during the motor imagery process, the alpha-high gamma PAC also shows strength change from pre- to post-imagery. Fig. 2C shows the coupling of phase of alpha oscillation and the envelope of gamma oscillation. Fig. 2C presents the PAC from alpha to various high gamma components. There is a clear decrease in PAC from approximately 0ms to 2500 ms, which is in a motor imagery block. The averaged PAC over frequencies from 70 Hz to 120 Hz in Fig. 2C is presented in Fig. 2D, and the temporal pattern of the averaged PAC is similar to the pattern
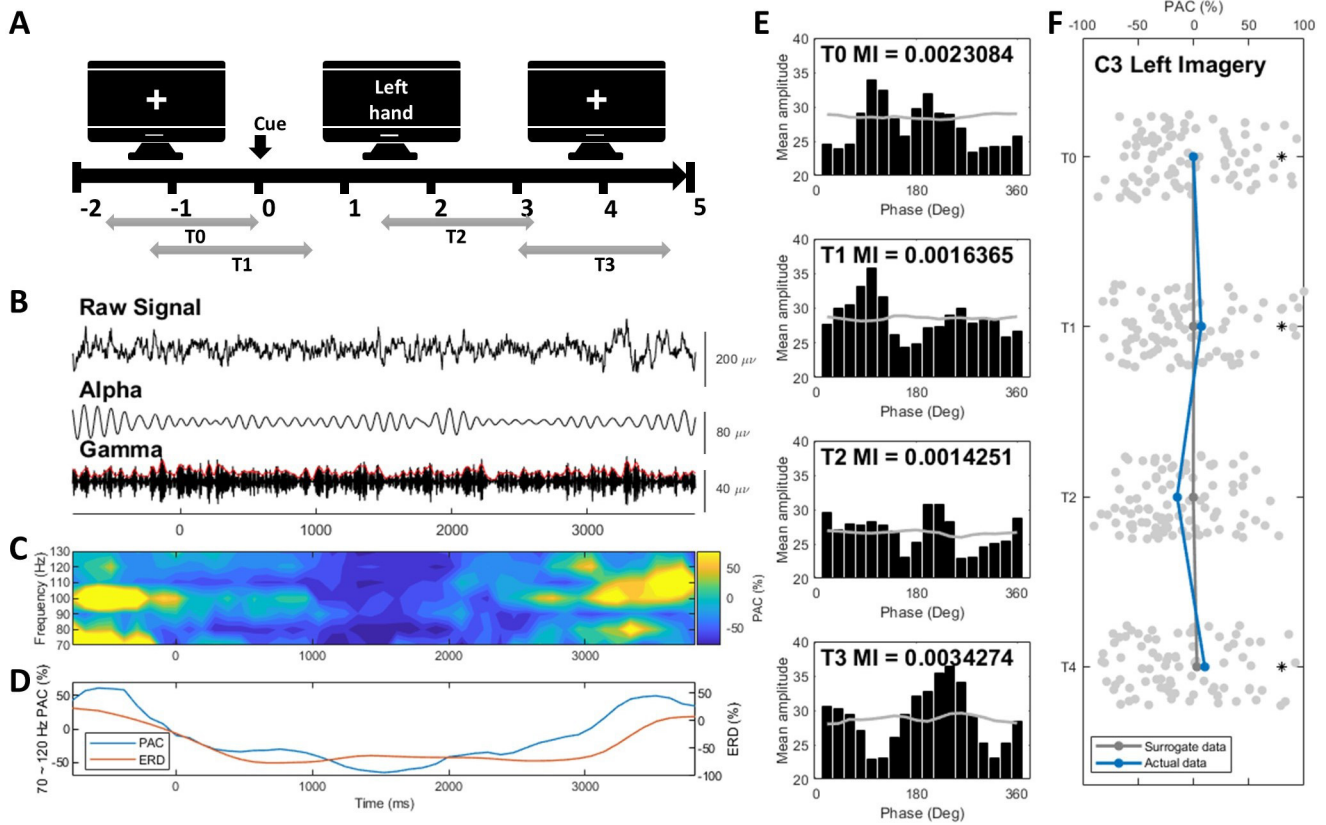
Fig 2. Exemplary trial during left hand imagery measured at the C3 electrode from a representative subject in dataset 1. (A) Illustration of a single trial in the motor imagery experiment. Bidirectional arrows represent the four intervals identified (*T0*: -1800–0 ms, *T1*: -1400–400 ms, *T2*: 600–2400 ms and *T3*: 3000–4800 ms). (B) The raw, Alpha (8–12 Hz) and high gamma (70–120 Hz) oscillation envelope (red). (C) PACs of alpha and high gamma rhythms over time. The PACs are presented in percentage, as the values are relative to PAC before the visual cue (0 ms). (D) The time series of alpha ERD and PAC averaged over frequencies (70 to 120 Hz) from the Fig. C. (E) Mean amplitude distributions of alpha-high gamma (70 – 120 Hz) PAC in time intervals (*T0, T1, T2* and *T3*). (*F*) Alpha-high gamma (70–120 Hz) over epochs. Statistical significance difference by Student's t test is marked with * (*p* < 0.05, comparison with *T2*). The gray lines on E and F represent the mean amplitude and MI from surrogate data respectively.

of ERD. The mean amplitude distribution shows consistently that such a PAC change is true. Fig. 2E shows the mean amplitude distribution of the four intervals identified: *T0* (-1800–0 ms), *T1* (-1400–400 ms), *T2* (600–2400 ms) and *T3* (3000–4800 ms), based on the cue (Fig. 2A). In contrast to other time intervals (*T0, T1,* and *T3*), the mean amplitude distribution of *T2* appears to be much closer to the uniform distribution which consequently yields a low MI. This decrease in PAC between alpha and high gamma during motor imagery was observed consistently over epochs, as shown in Fig. 2F. ANOVA test revealed that the MIs are significantly different over the four-time blocks (*T0*: 0.0024, *T1*: 0.0026, *T2*: 0.0021, *T3*: 0.0027, $F = 3.31$, $p < 0.05$) and Student's t test revealed that the MIs of T2 block and all other blocks are significantly different (*T0*: $p < 0.05$, $t = 2.29$; *T1*: $p < 0.05$, $t = 2.88$; *T3*: $p < 0.05$, $t = 2.93$).

In the analysis of the alpha ERD and alpha-high gamma PAC with all 52 subjects' data, we found a decrease in alpha power and alpha-high gamma PAC during motor imagery at *C3* and *C4* for both conditions (left- and right-hand imagery). Although there were subject variations, the average ERDs for left/right imagery were -48.94%/-52.24% at C3 and -49.83%/-46.64% at C4. Further, the PAC was -12.75%/-8.12% at C3 and -9.29%/-11.92% at C4 on average for left/right motor imagery (Fig. 3A). A one-sample *t*-test revealed that these decreases were statistically significant ($p < 0.05$, $t = -12.49/-12.43/-12.66/-13.08$ from C3L to C4R on ERD and $t = -9.68/-4.55/-7.39/-11.30$ from C3L to C4R on PAC). However, in pair-wise tests, there was no significant difference between left- versus right-hand imagery (C3/C4 of ERD: $p > 0.05$, $t = 2.04/-1.36$; C3/C4 of PAC: $p > 0.05$, $t = -2.46/1.79$).

Checking the presence of oscillation of phase frequency in amplitude frequency is important for a meaningful interpretation of the CFC pattern. Thus, we calculated the power spectral density (PSD) of high gamma amplitude as suggested in a study (Aru et al., 2015). The top figures in Fig. 3B present the normalized PSD of high gamma amplitude averaged over all subjects. As the alpha range shows consistent difference ($p < 0.05$, uncorrected) between the two-time blocks *T0* and *T2* in all conditions (C3L, C3R, C4L and C4R). The middle panel in Fig. 3B shows the mean amplitude of high gamma at each phase of alpha rhythm, which is also averaged over subjects. Clearly the mean amplitude decreases from *T0* to *T2* in all conditions and the distribution does not look uniform distribution, but closer to an unimodal distribution. Consequently, MI also decreases from T0 to T2 and the difference were significant (C3L: 0.0024 / 0.00209, $p < 0.05$, $t = 8.43$; C3R: 0.00231 / 0.00212, $p < 0.05$, $t = 4.17$; C4L: 0.00226 / 0.00204, $p < 0.05$, $t = 7.11$; C4R: 0.00231 / 0.00202, $p < 0.05$, $t = 10.07$). But surrogate data did not show a statistical difference between *T0* and *T2*. Comparing with alpha oscillation (the bottom in Fig. 3B), the mean amplitude of high gamma peaks between 0 and π radian phase of alpha oscillation.

3.2. Alpha ERD and alpha-high gamma PAC are correlated

Fig. 2E shows the temporal pattern of PAC is similar to that of ERD. To examine this similarity further, we investigated individual subject's temporal patterns of ERD and PAC and quantified the similarity between both measures using Pearson's correlation. The average of ERD and PAC over all subjects are presented in Fig. 4A. As shown, both ERD
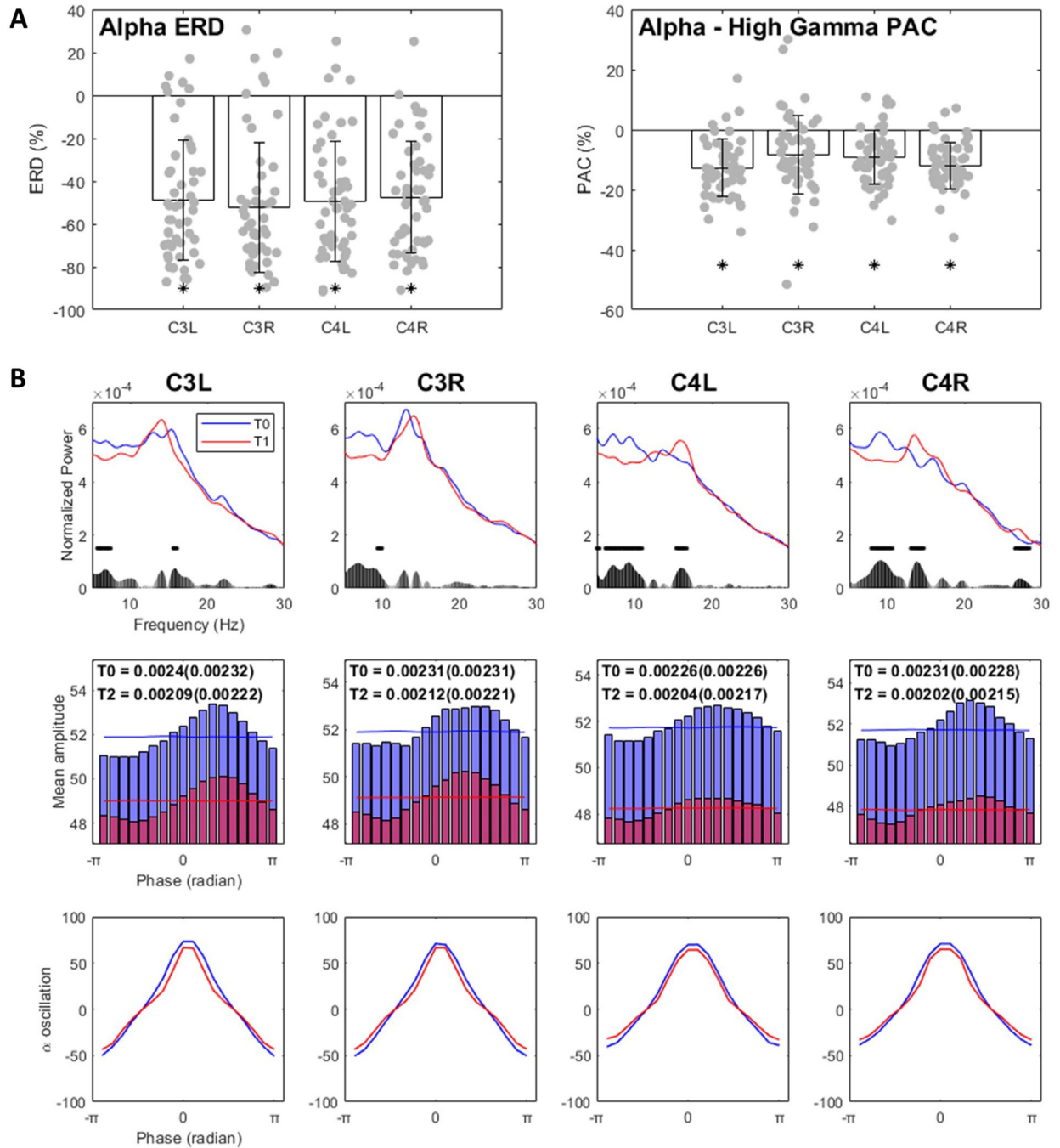
Fig 3. Alpha (8–12 Hz) ERDs and alpha-high gamma (70–120 Hz) PACs during the ready block (*T0*) and the motor imagery block (*T2*) from 52 subjects in dataset 1. (A) Distribution of ERDs and PACs in *T2* from 52 subjects. Every condition/electrode shows the negative mean value that was statistically significant with a one-sample *t*-test. However, no significant difference was observed for left versus right in ERD or PAC. Each bar graph is the mean of ERD or PAC and the vertical bar is the standard deviation. The circle represents each subject. The significance of the Student's t test is marked with * ($p < 0.05$). (B) Top, the normalized power spectral density of high gamma amplitude averaged over all subjects. The gray areas at the bottom represent the difference between *T0* and *T2*, *p* value was visualized by the intensity of gray color from light to dark ($p = 0$). The black dots represent statistically significant points ($p < 0.05$, uncorrected). Middle, The mean amplitudes for *T0* and *T2* respectively. The two lines represent the mean amplitude of surrogate data. The numbers in each figure denote the average modulation index (MI) of actual data and of surrogate data in parentheses. Bottom, The alpha oscillation was averaged over each of the phase from $-\pi$ to π radian. The blue represents *T0* and the red represents *T2*. C3L: Left imagery on electrode C3, C3R: Right imagery on electrode C3, C4L: Left imagery on electrode C4, C4R: Right imagery on electrode C4.

and PAC decreased during the imagery block and such decrease peaked at approximately the center of imagery block (roughly 1,500 ms). Then, both measures increased toward the baseline during post-imagery block (0%). Correlation coefficients were obtained and a histogram of subjects at each correlation coefficient was constructed. On average, every condition (electrodes and imagery types) showed a positive correlation. Interestingly, we observed a higher correlation (C3L: $r = 0.36$ with skewness = -0.70, C4R: $r = 0.29$ with skewness = -0.65) in the ipsilateral area than in the contralateral area (C3R: $r = 0.35$ with skewness = -0.86, C4L: $r = 0.42$ with skewness = -1.01), as shown in Fig. 4B.
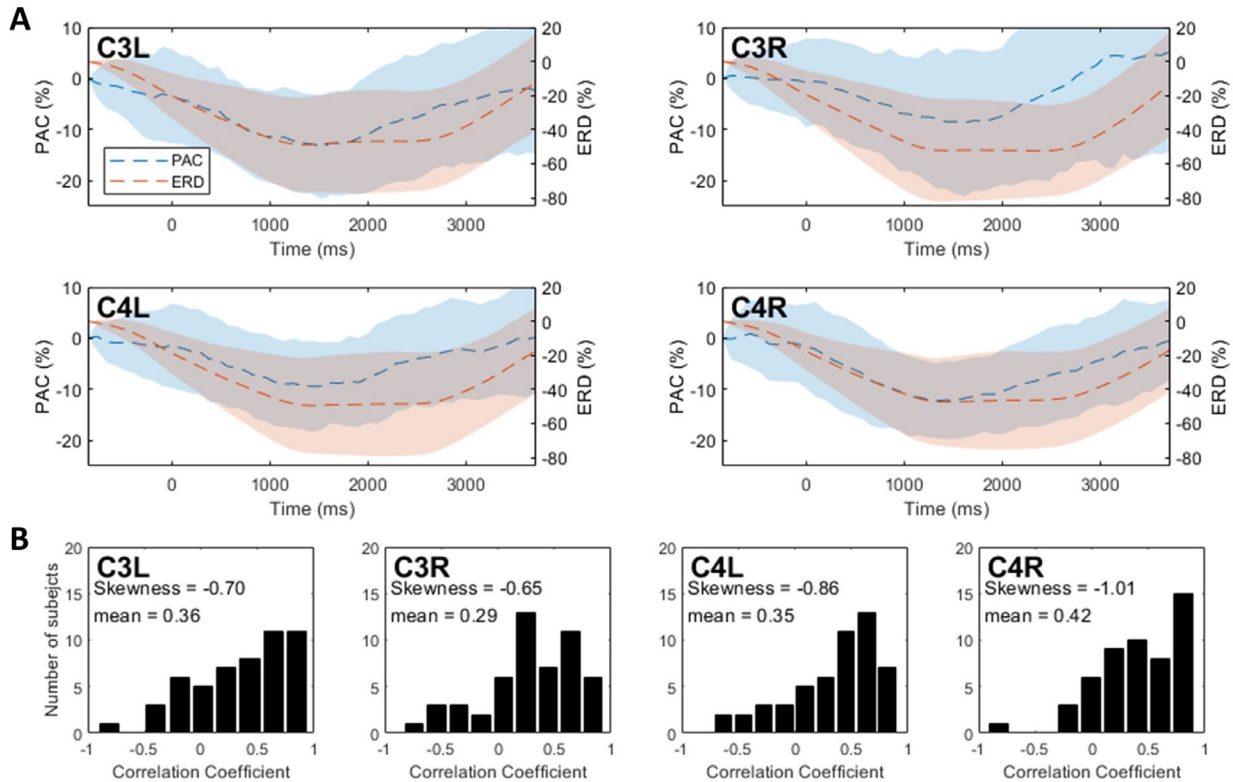
Fig 4. Correlation analysis between the time series of ERD and PAC. (A) Averaged ERD (red) and PAC (blue) from all subjects are shown for both condition and electrode locations. The transparent area in each figure represents the standard deviation. (B) Histograms of the correlation coefficients of ERD and PAC. The number of subjects that fell into each correlation coefficients range are presented. On the top-left of each figure, the mean correlation coefficient and the skewness of the distribution are presented.

Next, we investigated the association between two different times (*T0*: ready block and *T2*: imagery block). Simply the changes of alpha power (measured by ERD) and of MI (measured by PAC) at *T2*, which are the relative measure to the baseline, were compared with the magnitude of alpha power or MI at T0. Average values of four measures were calculated per each subject and the values from all subjects were plotted for each comparison. This process facilitates checking if a subject with higher/lower alpha or MI during the ready block (*T0*) shows a larger/smaller changes of alpha or MI during the imagery block (*T2*). The result is shown in Fig. 5.

As shown, subjects who exhibited higher alpha power during the ready produced a larger ERD in all conditions (C3 or C4 channels, left or right imagery), while the PAC during the imagery block showed no significant relation with alpha power during the ready block (Fig. 5A). In comparison with the MI during the ready block, the opposite result was observed (Fig. 5B). Subjects with a higher MI during the ready block showed a greater decrease in PAC during the imagery block while no relation was observed for MI during the ready and ERD during imagery. We quantified the extent to which they are related by Spearman's correlation analysis. Then, the outliers removed using the Mahalanobis distance. Alpha at T0 consistently showed the significant negative correlations with ERD at T2 for C3L (-0.532, $p < 0.05$), C3R (-0.506, $p < 0.05$), C4L (-0.453, $p < 0.05$) and C4R (-0.478, $p < 0.05$) respectively, while no significant correlations were observed with the PAC (in the bottom row in Fig. 5A). Such significant negative correlations were also observed between the MI at T0 and PAC at T2 for C3L (-0.618, $p < 0.05$), C3R (-0.415, $p < 0.05$), C4L (-0.496, $p < 0.05$) and C4R (-0.447, $p < 0.05$).

### 3.3. Major phase frequency for imagery types varies

Our next question was how does the PAC differ across imagination types (left or right motor imagery) and to what extent imagination types can be predicted by PAC. Unfortunately, no significant difference of alpha-high gamma PAC was observed between the two imagery types in Fig. 3. However, as PAC modulation may vary across subjects for imagery types, a rigorous and detailed analysis is necessary. Therefore, we expanded PAC analysis to various phase frequencies to see how differently they modulate the high-gamma amplitude especially related to imagination types. Thus, five phase frequencies were defined; *F1* (4–8 Hz), *F2* (8–12 Hz), *F3* (12–20 Hz), *F4* (20–28 Hz), and *F5* (28–40 Hz), and its coupling with high gamma activity was analyzed.

Fig. 6A presents the mean PACs of subjects when different phase frequencies were used. Circles denote subjects and those that differed statistically in the left versus right comparison are marked with filled circles. As shown, every phase frequency indicates that the distribution of most subjects is dense in the third quadrant (Fig. 6A), indicating a decrease in PAC during the imagery block (*T2*) compared to the ready block (*T0*). In addition, significant numbers of subjects were found in every phase frequency, although to a different degree. The numbers of significant subjects (FDR-corrected) were 8, 8, 5, 3, and 8 at the C3 electrode and 8, 6, 6, 6, and 8 at the C4 electrode as shown in Fig. 6B. Interestingly, we observed that the distribution of left imagery became more similar to that of right imagery as a higher phase frequency was used. Correlation analysis revealed that the quantified similarities of the two distributions at the C3/C4 electrodes are 0.1474/0.3271, 0.1095/0.0508, 0.03464/0.5654, 0.4693/0.5911 and 0.6421/0.5357 from the first (*F1*) to the last phase frequency (F5), as shown in Fig. 6C. The statistically significant correlation coefficient ($p < 0.05$, corrected) was observed in most frequencies except for F1 and F2 for C3 and F2 for C4.

Next, we performed decoding analysis using the PACs feature to predict imagination types (left or right). Decoding accuracy was estimated by a conventional machine learning approach that calculates a statistical
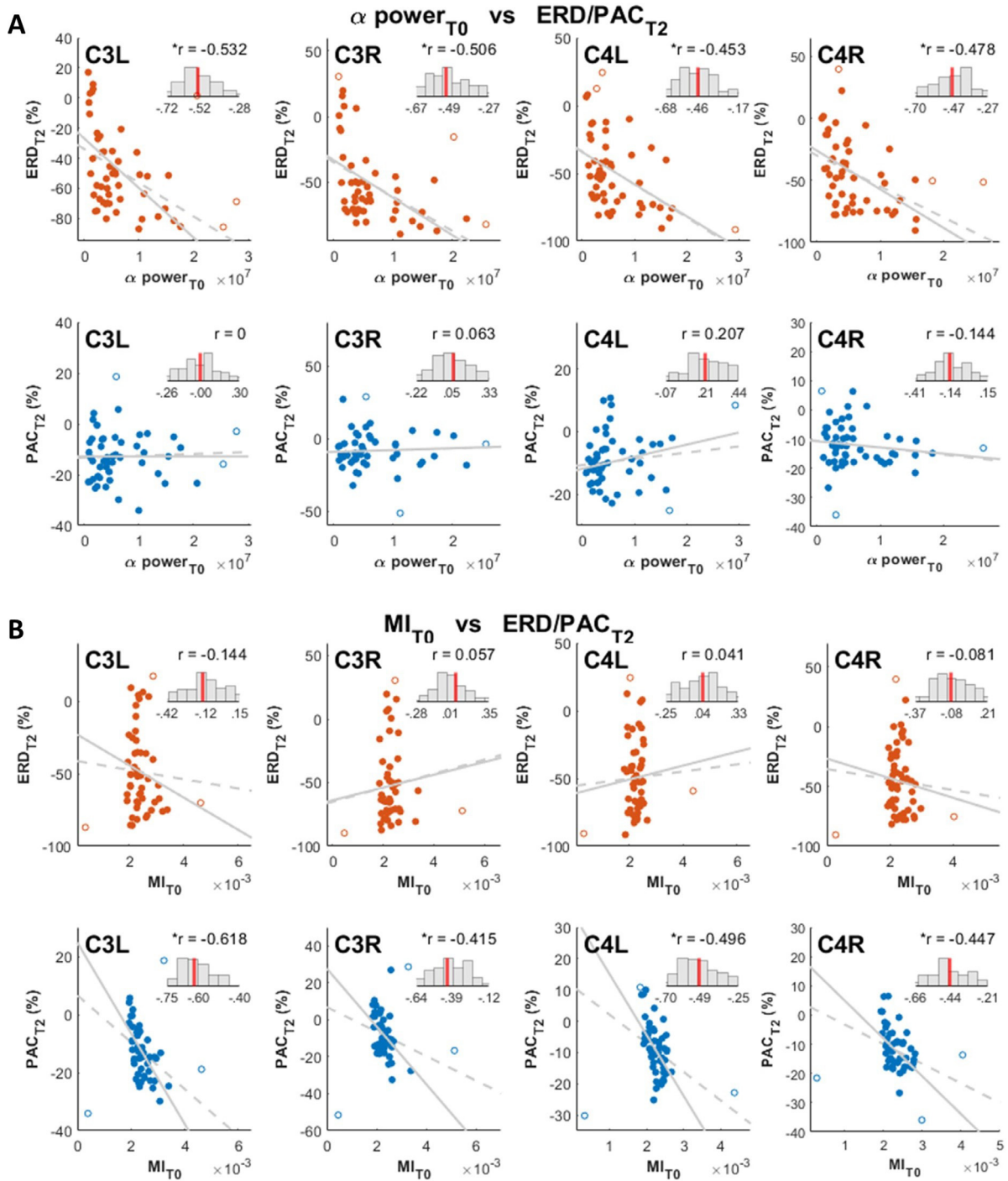
Fig 5. Association between the ready (*T0*) and imagery (*T2*) blocks. (A) Comparison of alpha power at T0 and ERD or PAC at *T2*. (B) Comparison of MI at *T0* and ERD or PAC at *T2*. On each sub figure of (A) and (B), subjects are presented as circles. Open circle denotes outliers identified by Mahalanobis distance. The regression lines are also presented with solid (w/o outliers) and dashed (w/ outliers) gray lines. The r is Spearman's correlation coefficient on subjects (w/o outliers) with the significance *$p < 0.05$. The distribution of correlation coefficient from bootstrapping ($n = 100$, w/o outliers) is presented inside each sub figure. The red vertical line indicates the r in each figure and the numbers on the bottom are the 95% confidence limits (at the 2.5% and 97.5% points) and the mean (μ) of the distribution. As seen, the two values (r and μ) are very close, indicating the calculated r represents the relationship between two variables.

accuracy through cross validation technique as described in Section 2.4. Fig. 7 presents the DA of left versus right imagery types by PAC from five different phase frequencies. Each phase frequency showed, on average, 52.86/ 53.07% (*F1*), 52.39/ 52.26% (*F2*), 53.87/ 51.38% (*F3*), 52.01/ 51.01% (*F4*), and 52.26/ 52.01% (F5) for the C3/C4 electrodes, which is considered around statistical chance level of 50.038%. However, the specific phase frequency that had the highest DA varied across subjects as shown in the middle panel of Fig. 7. Indeed, looking at the average of the subjects' maximum DAs, relatively high accuracies of 57.71 (C3) and 57.54 (C4) that are significantly higher than the statistical chance accuracy from surrogate data (C3: $p < 0.05$, $t = -2.12$; C4: $p < 0.05$, $t = -2.46$), were obtained, while the average of the mean DAs was still around the chance level (C3: 52.48%, C4: 51.94%, not significant $p > 0.05$ compared to statistical chance accuracy).
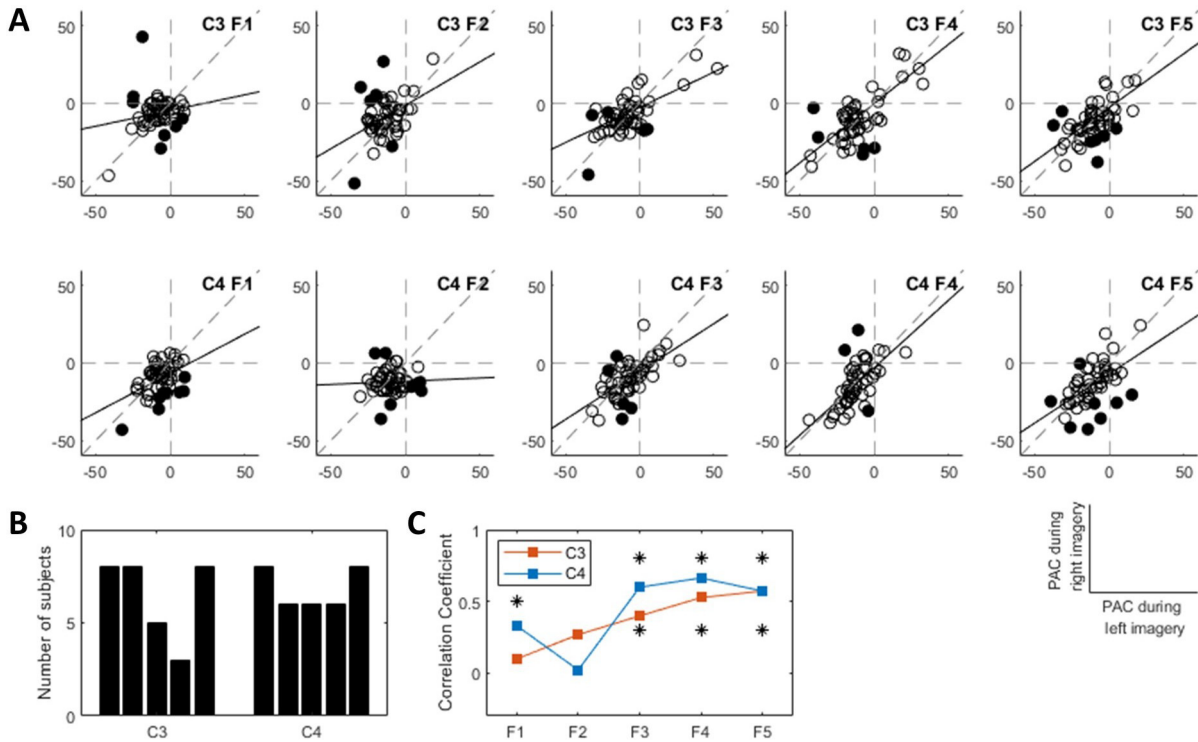
Fig 6. PACs of left and right imagery over various phase frequencies. (A) Mean PACs from C3 electrodes and C4 electrodes. Circles denote subjects' mean PACs and filled circles represent those that differed significantly in the left versus right comparison (FDR corrected). Lines for X = Y and the regression analysis are overlaid. *F1–F5* denote the interval of phase frequencies; *F1*; 4–8 Hz, *F2*; 8–12 Hz, *F3*; 12–20 Hz, *F4*; 20–28 Hz, *F1*; 28–40 Hz. (B) The numbers of significant subjects for *F1–F5*. (C) Correlation coefficient (r) for two PAC distributions of left/right imagery. Statistical significance is marked with * ($p < 0.05$).

To sum up, we observed that none of phase frequencies show the perfect discrimination of imagination types for every subject. Instead, a major frequency band that contributes to imagery types, seems differ across subjects and consequently, results in varying decoding accuracy across phase frequencies. Therefore, the subject-specific phase frequency should be identified beforehand and then applied or optimized to decode imagery types.

3.4. WCFC increases discriminativeness of imagery types

We observed that decoding accuracy varied across subjects and the major phase frequency with the highest accuracy was inconsistent. To solve this problem, we proposed a novel optimization approach weighting various cross-frequency couplings. In a simulation study, we confirmed that the proposed WCFC performed well in various scenarios (please refer to Fig. S2 in the supplementary material). Then we evaluated the method with two different datasets. Fig. 8 presents the decoding accuracies of methods tested. For the C3/C4 electrodes, BrPSD and NRPSD showed only 55.19/55.65% and 55.98/56.64%. However, the proposed method (WCFC1) yielded 61.98/65.80%, and WCFC2 that combined two electrodes showed 69.49%. This is very comparable to the conventional method (CSP), which resulted in 70.24%. A statistical test revealed that the difference between WCFC2 and CSP was not significant ($p = 0.5437$, $t = -0.61$).

In the analysis of dataset 2, three methods showed 49.09/50.75% (NrPSD), 59.25/62.39% (WCFC1) and 69.11% (WCFC2) on average. We confirmed again that the proposed WCFC outperforms NrPSD, which uses only the power feature (C3/C4 on BrPSD: $p < 0.05$, $t = -4.24/-6.84$; C3/C4 on NrPSD: $p < 0.05$ $t = -3.95/-6.04$).

Weights of the WCFC projection matrix constructed were investigated further to identify the contributing frequencies. Based on the classification accuracies by WCFC with the C4 electrode and CSP with 64 electrodes, we divided the subjects into two groups. Subjects who

demonstrated higher accuracy in the WCFC were categorized as the WCFC-dominant group, and those who showed better accuracy in CSP were categorized as the CSP-dominant group. The average accuracies (WCFC/CSP) of the two groups were 68.24/ 56.91% (WCFC dominant) and 60.92/ 73.11% (CSP-dominant). Fig. 9 illustrates the normalized average weight vectors of the WCFC projection matrices for the two groups. The weight vector of each subject was obtained by averaging the eight projection vectors, which are the first four and the last four vectors in the subject's projection matrix, because these are relatively significant vectors with higher Eigen values in discriminating two conditions (left and right imagery). Thus, each value in the weight vector can be seen as a kind of contribution score of each frequency. The weight overall was greater in the low frequency band than in the high frequency band. The average weights are shown at the bottom of Fig. 9. Both groups showed similar patterns in the low frequency range, while the WCFC-dominant group showed higher weights in high frequencies (e.g., amplitude frequency) than did the CSP-dominant group. Particularly, 90–130 Hz showed a statistically significant difference. These results are consistent with the other results, in which the phase-amplitude coupling can vary from subject to subject.

4. Discussion

### 4.1. Alpha-high gamma PAC in motor imagery

The alpha rhythm is associated with movement execution, imagery, and observation, and indeed, the alpha power decreases around the movement event and then rebounds returning back to the baseline (Nam et al., 2011; Pfurtscheller and Lopes da Silva, 1999; Yuan et al., 2010). Thus, this rhythm is at the center of research to understand motor function and has become the key feature in building a brain-computer interface (e.g., motor imagery-based brain-computer interface). However, the cross-frequency coupling during motor imagery has not been
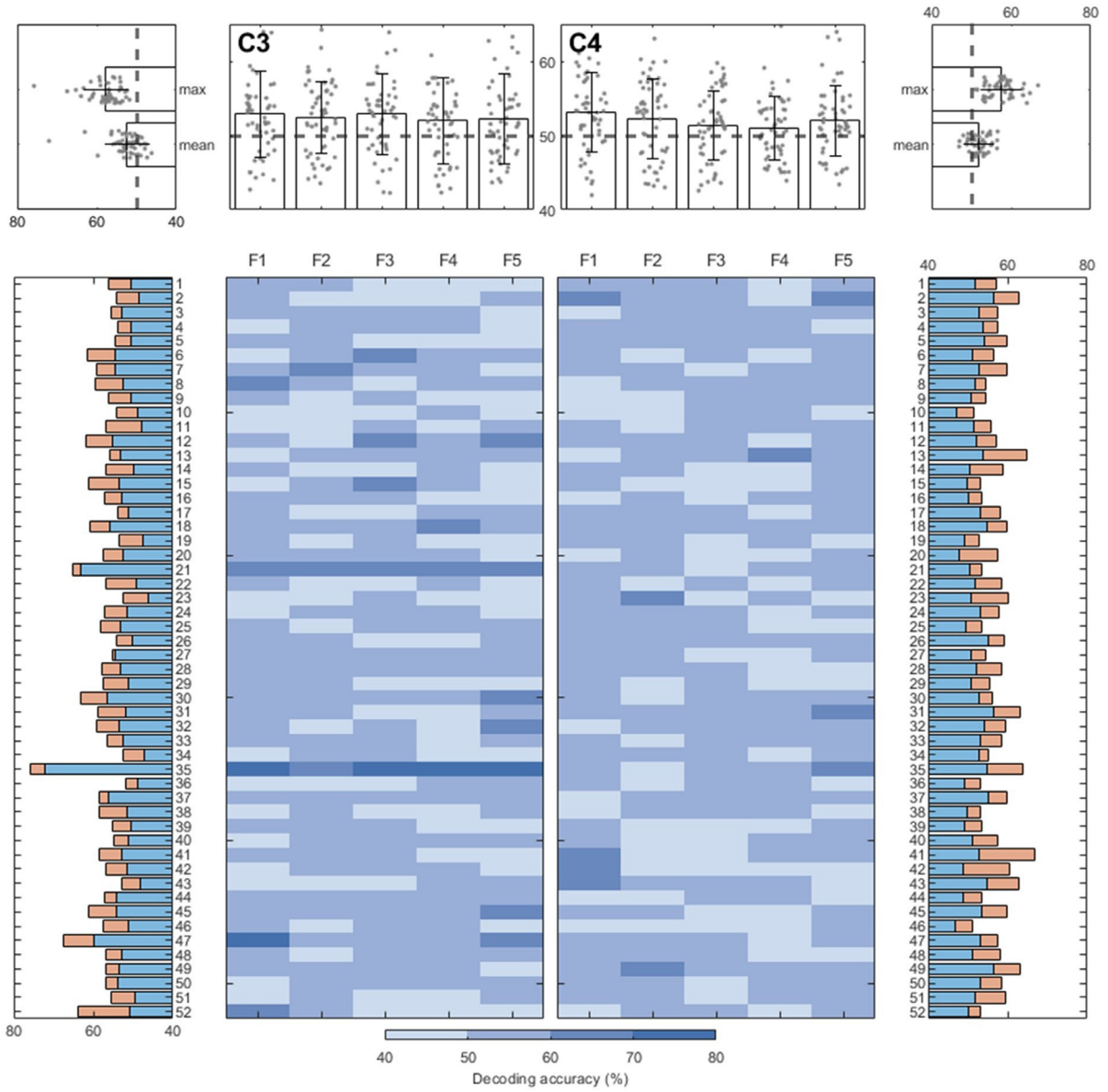
Fig 7. Decoding accuracy (DA) of five phase frequencies. The DA of each phase frequency computed with a 10×10-fold cross-validation is shown in the middle panel. The DA scale ranges from low (aqua blue) to high (deep blue). Mean (blue bar) and max DAs (orange bar) are presented for each subject (on both left/right sides) and each phase frequency (on top-middle panel). On the top-left/right sides, the averages across the subjects are shown for the mean DA and max DA with standard deviations. The horizontal dotted line represents statistical chance accuracy (50.038%), and the y-axis range of all graphs is the same.
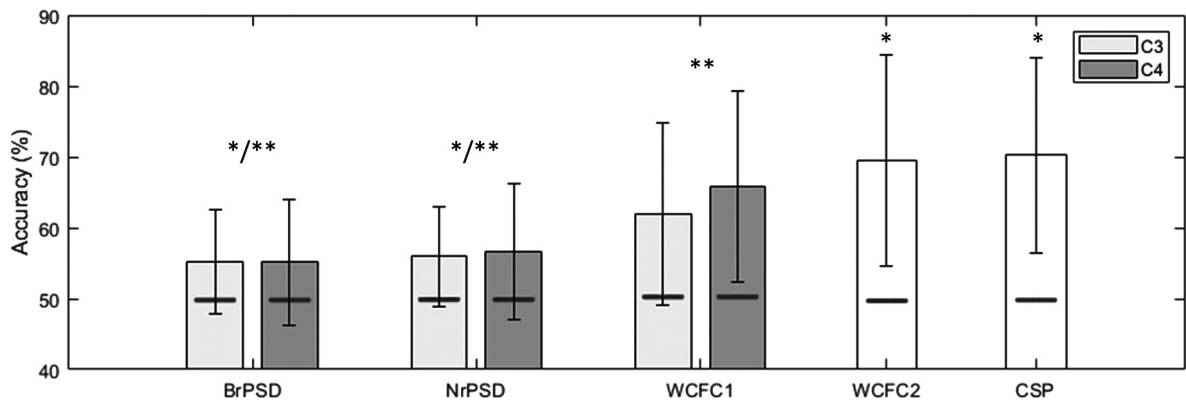
Fig 8. Comparison of the mean accuracies (%) of BrPSD, NrPSD, WCFC1, WCFC2 and CSP in dataset 1 (*N* = 52). Means and standard deviations of the accuracies are shown. The thick gray line on each bar represents the statistical chance accuracy (BrPSD: 49.09%, NrPSD: 49.81%, WCFC1: 49.36 %, WCFC2: 49.95% and CSP: 50.60%). Statistical significance performed by a Student's t-test is marked with * ($p < 0.001$, comparison with WCFC1) and ** ($p < 0.005$, with CSP).
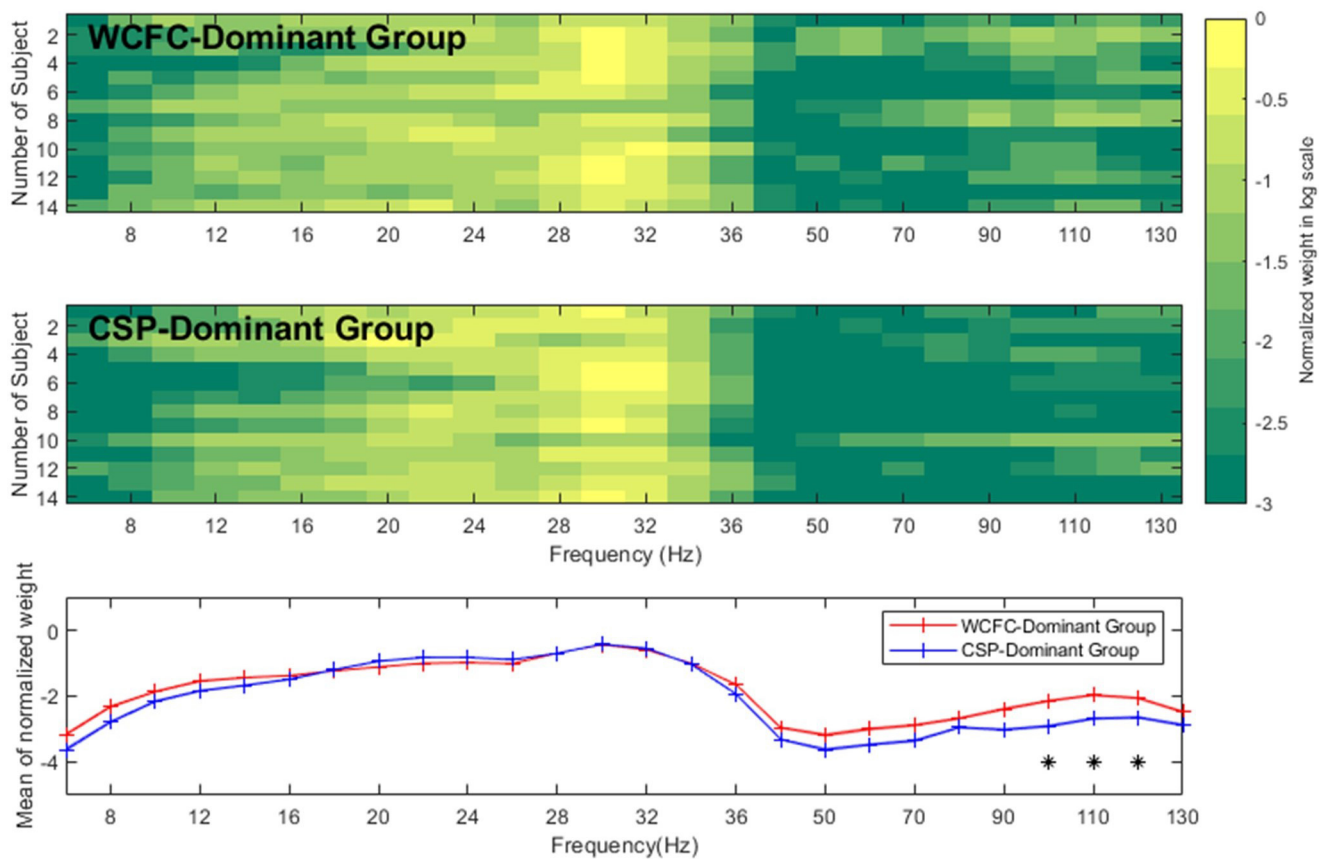
Fig 9. Normalized weights from the projection matrix for the WCFC- or CSP-dominant groups. The figure at the top is the weights in log scale for the WCFC-dominant group, and the middle figure is for the CSP-dominant group. The bottom figure is the mean weight in each group. The significant frequency bands by the Wilcoxon signed rank test are marked with * ($p < 0.05$).

investigated thoroughly and is understood less. In this study, we demonstrated that alpha-high gamma PAC is also associated with motor function and specifically, decreased during motor imagery compared to the ready state. Interestingly the temporal pattern of the PAC change correlated positively with the ERD pattern. This result indicates that the mechanisms of PAC and ERD may be similar.

The task-related desynchronization of neural oscillation is thought as being caused by independent neuronal activities in which the neurons become asynchronous. From the perspective of information theory, ERD is a state with high information, while consecutive ERS represents a less informative state, is the 'idling' state in the nervous system (Pfurtscheller et al., 1996). Similarly, the phase amplitude coupling within the same area, can be interpreted as a condition change from strong to loose interaction of the two frequencies because of the weakened alpha oscillator (Canolty and Knight, 2010), and argument previous studies have supported. Similarly, Combrisson and colleagues (2017) investigated the phase amplitude coupling from the standpoint of preparation and execution through a delayed motor task and found prominent alpha-gamma PAC during the delay period that disappeared during movement execution. They argued that such alpha-gamma phase amplitude coupling is replaced by delta-gamma phase amplitude coupling at execution, and phase amplitude coupling presents across wider brain areas beyond the primary motor areas.

Another noteworthy result is that the temporal patterns of PAC and ERD were similar, particularly in the ipsilateral area. As presented in Fig. 4B, the higher correlation was observed on electrode C3 for left-hand motor imagery (C3L: skewness = -0.7 and mean = 0.36) and on C4 during right-hand motor imagery (C4R: skewness = -1.01 and mean = 0.42). This implicates the tighter interaction of PAC and ERD

in the ipsilateral area and indicates the lateralization of such an interaction according to types of motor imagery (e.g., left and right), although the role of the ipsilateral area contributing to the interaction between ERD and PAC, is unclear. In general, alpha and beta ERD during motor imagery are dominant in the contralateral area (Nam et al., 2011). However, recent evidence has revealed the important association of ipsilateral hemisphere with motor behavior. A fMRI study demonstrated ipsilateral involvement of the primary motor cortex during motor imagery and execution (Porro et al., 2000), and another recent study also reported increased bilateral connectivity with ipsilateral sensorimotor cortices during coordination of multiple joints, which is a relatively complex movement (Wilkins and Yao, 2020). Thus, the important role of ipsilateral hemisphere seems very evident. Indeed, lesioning ipsilateral M1 in monkeys leads to a behavioral deficit (Bashir et al., 2012) and perturbation to ipsilateral M1 via TMS has been shown to increase task errors in human studies (Avanzino et al., 2008; Chen et al., 1997; Davare et al., 2007). Summarizing these results, the ipsilateral area appears to play an important role in motor behavior, although the specific neural mechanism regarding to the role of the ipsilateral hemisphere is still unknown.

We observed that the alpha-high gamma MI is larger in the ready state compared to the imagery state and that the gamma amplitude is maximal around between 0 and π phase of alpha oscillation (Fig. 3B). In previous studies, the association of the low frequency to the performance of movement tasks, has been shown (Engel and Fries, 2010; Gilbertson et al., 2005; Haegens et al., 2011), which indicates that cross-frequency coupling might contribute to motor function by modulating the high gamma amplitude. In the same line, some studies reported the importance of neural activity during preparation that relates

to the coming neural activity of movement (Churchland et al., 2010; Yanagisawa et al., 2012). Specifically, the stronger the phase amplitude coupling during preparation might provide an initial state for the activation of the high gamma amplitude to represent the information of motor function. Yanagisawa and colleagues (2012) showed that high gamma (80–150 Hz) amplitude is modulated at the trough of the alpha rhythm (10–14 Hz) during the waiting period and this phase-locked state is released in the movement execution, and they introduced a "hold-and-release" model to explain such an observation. This is consistent with our result that presents the larger the phase amplitude coupling during ready state and the decrease of the phase amplitude coupling during imagery state. But in contrast, the amplitude of gamma was high around the crest of the alpha oscillation in this study (Fig. 3B), which is similar to other studies (Connolly et al., 2015; Yang et al., 2014). Obviously, further investigation of the lock phase and its role is important and necessary for a better understanding of the neural mechanism of motor function. To sum up, the phase amplitude coupling serves functions in motor preparation and seems to play an important role for the ongoing neural dynamics of movement tasks. Previous studies on the phase amplitude coupling have focused mostly on the invasive recordings and motor execution, while our study demonstrate that such coupling can be extended to the motor imagery and non-invasive recording.

Another noteworthy point is that the phase amplitude coupling can be over-estimated due to the irregularity of physiological oscillations that are related to non-stationarity, variant SNR or power, non-sinusoidal waveform and sharp waves (Aru et al., 2015; Cole and Voytek, 2017; Gerber et al., 2016; Lozano-Soldevilla et al., 2016). Thus, it is highly recommended to be cautious about the misinterpretation from spurious the phase amplitude coupling. Regarding this issue, A comprehensive review on the concerns of the phase amplitude coupling was summarized and recommendations were provided for reliable the phase amplitude coupling analysis by Aru et al (2015). The suggested first step is to check for the presence of oscillation that can be relatively easily performed by PSD analysis. In our study, this was investigated (Fig. 3B top) and we confirmed that the alpha range shows a higher power in the ready block ($T0$) than in the imagery block ($T2$). Based on the result, the phase frequency (8–12 Hz) seems to include the meaningful frequency range and we think that the bandwidths for phase and amplitude frequencies also fairly follow the recommendation of "*narrow enough for phase frequency and large enough for amplitude frequency*" (Aru et al., 2015). Second, the power or SNR of bands may influence the phase amplitude coupling estimation (Aru et al., 2015; Muthukumaraswamy and Singh, 2011). To prevent this, selecting a subset of trials in which the distribution of power across trials is identical, is suggested (Aru et al., 2015; Schoffelen et al., 2005).

In this study, IQR was introduced to remove outlier epochs and signals were baseline corrected by EMD as was proposed to obtain promising oscillations for the phase amplitude coupling computation (Yeh and Shi, 2018). These methods could reduce the factors that contribute to spurious the phase amplitude coupling, although it is not perfect. However, this may not be sufficient because identical power is not true across different times within an epoch even though the power and SNR were corrected across epochs. Alpha oscillation decreases during motor imagery compared to ready block. Thus, additional analysis is required to confirm that the decrease of PAC in the imagery block is not a byproduct of alpha dynamics. One obvious way to answer this is to test the PACs of two time blocks that are showing different power levels, but with broken coupling. If the observation of PAC is from the power changes of alpha oscillation, then MIs from surrogate data should also show a significant difference between the ready and imagery blocks. However, it turns out that surrogate data do not show such a difference (Fig. 3B middle). This indicates that the initial observation of the decreased PAC during imagery is trustable. Additionally, we conducted a further simulation study for checking whether power change in phase frequency influences the estimation of modulation index. From the investigation with signals of two different groups (alpha amplitude in one group is larger than an-

other group.), we found that a subtle difference may present due to the power change of alpha oscillation (Fig. S5 in supplementary material). However, such difference was not statistically significant ($p = 0.2171$, $t = -1.2383$). Thus, we believe that it is not likely that PAC decrease is due to the change of alpha power.

4.2. Association between motor preparation and imagery

In Fig 5, we observed the interesting temporal association between $T0$ (ready) to $T2$ (imagery). The time interval T0 is the state in which subjects wait for the coming instructions on the direction of motor imagery. Thus, it is considered not to be a pure resting state, but motor preparation that requires active engagement in the task. In this context, the high correlation between the two time intervals is very interesting. Our finding of the association between alpha power at $T0$ and ERD at $T2$ is consistent with that in previous studies. A similar motor imagery study investigated the somatosensory rhythm (SMR), which includes the alpha frequency, and demonstrated that trials with a higher pre-cue SMR amplitude yielded significantly better classification performance than trials with lower SMR amplitude (Maeder et al., 2012). This indicates that alpha rhythms during motor preparation influence the quality of motor imagery in the context of lateralization. Similarly, a higher alpha amplitude or alpha network during the resting state is reported as the key feature for people who modulate the detectable and classifiable alpha ERD during motor imagery (Ahn et al., 2013; Blankertz et al., 2010) or to predict imagery performance (Bauer et al., 2015).

In this context, cross-frequency coupling during preparation is also considered important in estimating the degree of PAC change during motor imagery. Practically, we think that this information of alpha power and MI during motor preparation may be useful in predicting the quality of ongoing motor imagery that is very important aspect in brain-computer interface. In addition, these could also possibly be used to predict BCI literacy because it can be considered an inherent characteristic of an individual.

4.3. Applicability of WCFC

We demonstrated the association between the phase amplitude coupling and motor function and proposed a novel method that can extract the most discriminative information from multiple frequencies. In general, previous algorithms that quantify phase-frequency coupling (Canolty et al., 2006; Meij et al., 2012, 2012; Munia and Aviyente, 2019; Penny et al., 2008; Tort et al., 2010; van Wijk et al., 2015; Voytek et al., 2013), have not taken powers of frequencies into account. This is true and obvious because they were designed to estimate only the phase-amplitude coupling of two frequencies. Consequently, they are less useful in classifying different conditions. However, WCFC is an algorithm that optimizes the linear combination of both frequency couplings and band powers by using the multi-frequency covariance matrix, which is referred as the CFC matrix here. This was proven to be true in the analysis of the projection vector (Fig. 8). The filters in the group that performed well in classification were weighted not only at low frequencies but also at high frequencies, while the groups that performed poorly showed a small weight at high frequencies. Thus, we expected that WCFC is capable to classify motor imagery types efficiently and effectively. From the computational study, we confirmed our initial expectation by checking the performance of WCFC with two datasets. In dataset 1, the WCFC yielded performance (69.49%) to the conventional algorithm (70.24%) in the BCI field with no statistically significant difference ($p > 0.05$), as shown in Fig. 8. Interestingly, only two electrodes were used in WCFC while CSP used signals from all 64 electrodes. In dataset 2 from BCI Competition IV, WCFC2 showed reasonable performance (69.11%, Kappa value = 0.38) in the ranking (Kappa value of 5th place team = 0.37) although we employed the conventional linear classifier to classify based on the WCFC features. This is a remarkable result in the context of classification accuracy and reveals the strength

Table 1

Comparison of the mean accuracies (%) of NrPSD (statistical chance level 50.44%), WCFC1 (statistical chance level 49.42%) and WCFC2 (statistical chance level 51.78%, kappa value 0.0343) in dataset 2 ($N = 9$).

	NrPSD		WCFC1		WCFC2	
	C3	C4	C3	C4	Accuracy (%)	Kappa value
S1	52.19	52.19	49.12	58.77	56.14	0.1345
S2	49.80	46.12	51.84	50.61	53.88	0.0752
S3	47.83	51.30	59.57	55.22	61.74	0.2254
S4	52.77	49.84	67.75	63.84	75.57	0.5115
S5	49.08	50.92	67.77	67.40	76.19	0.5270
S6	51.00	51.00	52.99	54.18	52.19	0.0314
S7	46.12	51.72	60.34	64.66	83.19	0.6640
S8	45.65	53.04	62.61	78.26	78.83	0.5591
S9	47.35	50.61	61.61	68.57	85.31	0.7061
Mean	49.09 */**	50.75 */**	59.25 **	62.39 **	69.11*	0.3816

Statistical significance performed by a Wilcoxon signed-rank test is marked with *(C3/C4 of NrPSD: $p < 0.05$, $t = $ -2.31/-2.66 comparison with WCFC1; WCFC2: $p < 0.05$, $t = $ -2.07 with C4 of WCFC1) and ** (C3/C4 of NrPSD: $p < 0.05$, $t = $ -2.66/-2.66; C3/C4 of WCFC1: $p < 0.05$, $t = $ -2.54/-2.07 with WCFC2).

of WCFC. However, we also highlighted that it was a successful attempt to combine the two important feature types (power and coupling). In Fig. 7, we failed to achieve a reasonable performance (like 70% on average) with a single PAC computed by the modulation index. However, the transformed feature resulting from a linear combination of various frequency components yielded a better decoding accuracy. This indicates that information may scatter over various components and both biomarker types should be considered together. Ultimately, we expect that machine learning can be utilized for such analysis. Regarding the performance achieved by WCFC, 70% accuracy looks low. However, we believe that the performance of WCFC can be increased with recent advanced classifiers (e.g., convolutional neural network, random forest model, etc.) (Akram et al., 2015; Lawhern et al., 2018) or computing WCFC over multiple electrodes.

Given these results, WCFC is an effective and practically useful algorithm, as there are situations in which many electrodes are unavailable. Usually, consumer-grade EEG headsets do not provide many electrodes, and thus, in this case, WCFC can be applied to decode mental states or imagery conditions. Another domain that WCFC can be used is the deep brain stimulation in brain disease. Recent studies have investigated the feasibility of the closed loop in deep brain stimulation, which reads continuous neural signals inside the brain and determines the optimized parameter or the timing for stimulation based on biomarkers (Beudel and Brown, 2016; Bocci et al., 2019). However, the number of electrodes is limited and only 1 to 4 electrodes are available depending upon the DBS setting. Despite this constraint, WCFC can maximize the information from the band power and also couplings across various frequencies. Indeed, both amplitude and the phase amplitude coupling are reported to be promising biomarkers and potential candidates for adaptive DBS (Bahramisharif et al., 2016; Goodman et al., 2018; Hemptinne et al., 2013; Kondylis et al., 2016; Malekmohammadi et al., 2018). In conclusion, we believe that the proposed WCFC method is practically applicable in the scenarios above Table 1.

4.4. Limitations of the study

In this section, we discuss the limitations of this study, and some possible future work.

First, motor function is related not only to one area in the brain, but involves various areas, such as the sensorimotor cortex, striatum, thalamus, and supplementary motor area (Mtui et al., 2020). Indeed, ERD is reported to be triggered by the decreased excitability of thalamic reticular nucleus cells by the thalamo-cortical network (Suffczynski, 1999). The phase amplitude coupling is considered to be the result of the coupling between the motor cortex and subthalamic nucleus (STN) caused by cortico-basal ganglia network (Lalo et al., 2008). Bichsel and colleagues (2018) also suggested for Parkinson's disease that the coupling between the alpha phase of basal ganglia and the gamma amplitude of the motor cortex is related to movement in the goal-direct movement and it is related to the movement function of the sensorimotor cortico-basal ganglia circuit (Bichsel et al., 2018). Given these reports, it appears that the same motor network may cause the phase amplitude coupling and ERD. Consistent with this idea, we presented strong evidence showing the high temporal correlation between the two measures. However, our interpretation is somewhat limited as we used signals recorded only from the scalp. Thus, an in-depth analysis with local field potentials recorded from the basal ganglia network would provide strong evidence of the origin, or relation between ERD and PAC.

We proposed a novel method to extract the most informative and discriminative features by combining power and couplings across frequencies. As a result, the proposed method showed performance comparable to the conventional method that uses all possible electrodes. In addition, we found that higher frequency is important in WCFC-dominant groups. However, WCFC did not show good performance in the CSP-dominant group. This implies that WCFC may be effective for subjects who do not show visible information about cross-frequency coupling during motor imagery. For this type of subject, it may be better to use the band-power based standard method (e.g., CSP) or coupling across multiple electrodes to uncover such invisible information or maximize relevant information. In general, multiple electrodes are available and combining their information probably is beneficial to increase classification accuracy. However, the WCFC formula proposed in this study cannot combine information from many electrodes, and we provided only a simple idea that concatenates feature vectors from two electrodes. In addition, we used only the C3 and C4 electrodes, which cover the motor area, but it is possible that different frequencies on two distant electrodes may give meaningful information. Previous studies have reported the relation between the phase amplitude coupling of the frontal regions and the posterior parietal region (Bertrand and Jerbi, 2009). Thus, methods to optimize information from multiple areas is another challenging issue to be resolved.

5. Conclusion

We have provided empirical evidence of the alpha-high gamma coupling during motor imagery, and such coupling is associated with changes in alpha power. In addition, a novel methodology was proposed that extracts the maximally discriminative information from multi-frequency components effectively and was proven to show excellent performance in classifying motor imagery types. We believe that our

results expand the knowledge of the motor network and pave the way for novel decoding methods of brain states classification that involve cross-frequency coupling.

Acknowledgement

Supplementary materials

Supplementary material associated with this article can be found, in the online version, at doi:10.1016/j.neuroimage.2021.118403.

Reference

Ahn, M., Cho, H., Ahn, S., Jun, S.C., 2013. High theta and low alpha powers may be indicative of BCI-illiteracy in motor imagery. PLoS One 8, e80886. doi:10.1371/journal.pone.0080886.

Akram, F., Han, S.M., Kim, T.-S., 2015. An efficient word typing P300-BCI system using a modified T9 interface and random forest classifier. Comput. Biol. Med. 56, 30–36. doi:10.1016/j.compbiomed.2014.10.021.

Al-Subari, K., Al-Baddai, S., Tomé, A.M., Volberg, G., Hammwöhner, R., Lang, E.W., 2015. Ensemble empirical mode decomposition analysis of EEG data collected during a contour integration task. PLoS One 10, e0119489. doi:10.1371/journal.pone.0119489.

Aru, Juhan, Aru, Jaan, Priesemann, V., Wibral, M., Lana, L., Pipa, G., Singer, W., Vicente, R., 2015. Untangling cross-frequency coupling in neuroscience. Curr. Opin. Neurobiol. SI 31, 51–61. doi:10.1016/j.conb.2014.08.002.

Avanzino, L., Bove, M., Trompetto, C., Tacchino, A., Ogliastro, C., Abbruzzese, G., 2008. 1-Hz repetitive TMS over ipsilateral motor cortex influences the performance of sequential finger movements of different complexity. Eur. J. Neurosci. 27, 1285–1291. doi:10.1111/j.1460-9568.2008.06086.x.

Axmacher, N., Henseler, M.M., Jensen, O., Weinreich, I., Elger, C.E., Fell, J., 2010. Cross-frequency coupling supports multi-item working memory in the human hippocampus. Proc. Natl Acad. Sci. 107, 3228–3233. doi:10.1073/pnas.0911531107.

Bahramisharif, A., Gerven, M.A.J., van, Aarnoutse, E.J., Mercier, M.R., Schwartz, T.H., Foxe, J.J., Ramsey, N.F., Jensen, O., 2013. Propagating neocortical gamma bursts are coordinated by traveling alpha waves. J. Neurosci. 33, 18849–18854. doi:10.1523/JNEUROSCI.2455-13.2013.

Bahramisharif, A., Mazaheri, A., Levar, N., Schuurman, P.R., Figee, M., Denys, D., 2016. Deep brain stimulation diminishes cross-frequency coupling in obsessive-compulsive disorder. Biol. Psychiatry 80, e57–e58. doi:10.1016/j.biopsych.2015.05.021.

Bashir, S., Kaeser, M., Wyss, A., Hamadjida, A., Liu, Y., Bloch, J., Brunet, J.-F., Belhaj-Saif, A., Rouiller, E.M., 2012. Short-term effects of unilateral lesion of the primary motor cortex (M1) on ipsilesional hand dexterity in adult macaque monkeys. Brain Struct. Funct. 217, 63–79. doi:10.1007/s00429-011-0327-8.

Bauer, R., Fels, M., Vukelić, M., Ziemann, U., Gharabaghi, A., 2015. Bridging the gap between motor imagery and motor execution with a brain–robot interface. Neuroimage 108, 319–327. doi:10.1016/j.neuroimage.2014.12.026.

Baumeister, J., Barthel, T., Geiss, K.R., Weiss, M., 2008. Influence of phosphatidylserine on cognitive performance and cortical activity after induced stress. Nutr. Neurosci. 11, 103–110. doi:10.1179/147683008X301478.

Benjamini, Y., Hochberg, Y., 1995. Controlling the false discovery rate: a practical and powerful approach to multiple testing. J. Royal Stat. Soc. 57, 289–300. doi:10.1111/j.2517-6161.1995.tb02031.x.

Bertrand, O., Jerbi, K., 2009. Cross-frequency coupling in parieto-frontal oscillatory networks during motor imagery revealed by magnetoencephalography. Front. Neurosci. 3. doi:10.3389/neuro.01.011.2009.

Beudel, M., Brown, P., 2016. Adaptive deep brain stimulation in Parkinson's disease. Parkinsonism & related disorders. In: Proceedings of XXI World Congress on Parkinson's Disease and Related Disorders, Milan, Italy, pp. S123–S126. doi:10.1016/j.parkreldis.2015.09.028 December 6-9, 201522.

Bichsel, O., Gassert, R., Stieglitz, L., Uhl, M., Baumann-Vogel, H., Waldvogel, D., Baumann, C.R., Imbach, L.L., 2018. Functionally separated networks for self-paced and externally-cued motor execution in Parkinson's disease: evidence from deep brain recordings in humans. Neuroimage 177, 20–29. doi:10.1016/j.neuroimage.2018.05.012.

Blankertz, B., Sannelli, C., Halder, S., Hammer, E.M., Kübler, A., Müller, K.-R., Curio, G., Dickhaus, T., 2010. Neurophysiological predictor of SMR-based BCI performance. Neuroimage 51, 1303–1309. doi:10.1016/j.neuroimage.2010.03.022.

Blankertz, B., Tomioka, R., Lemm, S., Kawanabe, M., Muller, K., 2008. Optimizing spatial filters for robust EEG single-trial analysis. IEEE Signal Process. Mag. 25, 41–56. doi:10.1109/MSP.2008.4408441.

Bocci, T., Arlotti, M., Marceglia, S., Prenassi, M., Ardolino, G., Cogiamanian, F., Borrellini, L., Rampini, P., Locatelli, M., Barbieri, S., Priori, A., 2019. Adaptive deep brain stimulation for Parkinson's disease: safety and effectiveness. Clin. Neurophysiol. 130, e17. doi:10.1016/j.clinph.2018.09.098.

Bruns, A., Eckhorn, R., 2004. Task-related coupling from high- to low-frequency signals among visual cortical areas in human subdural recordings. Int. J. Psychophysiol. 51, 97–116. doi:10.1016/j.ijpsycho.2003.07.001.

Canolty, R.T., Edwards, E., Dalal, S.S., Soltani, M., Nagarajan, S.S., Kirsch, H.E., Berger, M.S., Barbaro, N.M., Knight, R.T., 2006. High gamma power is phase-locked to theta oscillations in human neocortex. Science 313, 1626–1628. doi:10.1126/science.1128115.

Canolty, R.T., Knight, R.T., 2010. The functional role of cross-frequency coupling. Trends Cogn. Sci. 14, 506–515. doi:10.1016/j.tics.2010.09.001.

Chen, R., Gerloff, C., Hallett, M., Cohen, L.G., 1997. Involvement of the ipsilateral motor cortex in finger movements of different complexities. Ann. Neurol. 41, 247–254. doi:10.1002/ana.410410216.

Cho, H., Ahn, M., Ahn, S., Kwon, M., Jun, S.C., 2017. EEG datasets for motor imagery brain–computer interface. Gigascience 6. doi:10.1093/gigascience/gix034.

Churchland, M.M., Cunningham, J.P., Kaufman, M.T., Ryu, S.I., Shenoy, K.V., 2010. Cortical preparatory activity: representation of movement or first cog in a dynamical machine? Neuron 68, 387–400. doi:10.1016/j.neuron.2010.09.015.

Cohen, M.X., Elger, C.E., Fell, J., 2008. Oscillatory activity and phase–amplitude coupling in the human medial frontal cortex during decision making. J. Cogn. Neurosci. 21, 390–402. doi:10.1162/jocn.2008.21020.

Cole, S.R., Voytek, B., 2017. Brain oscillations and the importance of waveform shape. Trends Cogn. Sci. 21, 137–149. doi:10.1016/j.tics.2016.12.008.

Combrisson, E., Perrone-Bertolotti, M., Soto, J.L., Alamian, G., Kahane, P., Lachaux, J.-P., Guillot, A., Jerbi, K., 2017. From intentions to actions: neural oscillations encode motor processes through phase, amplitude and phase-amplitude coupling. Neuroimage 147, 473–487. doi:10.1016/j.neuroimage.2016.11.042.

Connolly, A.T., Jensen, A.L., Bello, E.M., Netoff, T.I., Baker, K.B., Johnson, M.D., Vitek, J.L., 2015. Modulations in oscillatory frequency and coupling in globus pallidus with increasing Parkinsonian severity. J. Neurosci. 35, 6231–6240. doi:10.1523/JNEUROSCI.4137-14.2015.

Davare, M., Duque, J., Vandermeeren, Y., Thonnard, J.-L., Olivier, E., 2007. Role of the ipsilateral primary motor cortex in controlling the timing of hand muscle recruitment. Cereb Cortex 17, 353–362. doi:10.1093/cercor/bhj152.

De Lange, F.P., Jensen, O., Bauer, M., Toni, I., 2008. Interactions between posterior gamma and frontal alpha/beta oscillations during imagined actions. Front. Hum. Neurosci. 2. doi:10.3389/neuro.09.007.2008.

De Maesschalck, R., Jouan-Rimbaud, D., Massart, D.L., 2000. The Mahalanobis distance. Chemom. Intell. Lab. Syst. 50, 1–18. doi:10.1016/S0169-7439(99)00047-7.

Engel, A.K., Fries, P., 2010. Beta-band oscillations—signalling the status quo? Curr. Opin. Neurobiol. Cogn. Neurosci. 20, 156–165. doi:10.1016/j.conb.2010.02.015.

Ermiş, E., Jungo, A., Poel, R., Blatti-Moreno, M., Meier, R., Knecht, U., Aebersold, D.M., Fix, M.K., Manser, P., Reyes, M., Herrmann, E., 2020. Fully automated brain resection cavity delineation for radiation target volume definition in glioblastoma patients using deep learning. Radiat. Oncol. 15, 100. doi:10.1186/s13014-020-01553-z.

Foster, J.J., Sutterer, D.W., Serences, J.T., Vogel, E.K., Awh, E., 2017. Alpha-band oscillations enable spatially and temporally resolved tracking of covert spatial attention. Psychol. Sci. 28, 929–941. doi:10.1177/0956797617699167.

Fu, R., Han, M., Tian, Y., Shi, P., 2020. Improvement motor imagery EEG classification based on sparse common spatial pattern and regularized discriminant analysis. J. Neurosci. Methods 343, 108833. doi:10.1016/j.jneumeth.2020.108833.

Genovese, C.R., Lazar, N.A., Nichols, T., 2002. Thresholding of statistical maps in functional neuroimaging using the false discovery rate. Neuroimage 15, 870–878. doi:10.1006/nimg.2001.1037.

Gerber, E.M., Sadeh, B., Ward, A., Knight, R.T., Deouell, L.Y., 2016. Non-sinusoidal activity can produce cross-frequency coupling in cortical signals in the absence of functional interaction between neural sources. PLoS One 11, e0167351. doi:10.1371/journal.pone.0167351.

Gilbertson, T., Lalo, E., Doyle, L., Lazzaro, V.D., Cioni, B., Brown, P., 2005. Existing motor state is favored at the expense of new movement during 13–35 HZ oscillatory synchrony in the human corticospinal system. J. Neurosci. 25, 7771–7779. doi:10.1523/JNEUROSCI.1762-05.2005.

Goodman, M.S., Kumar, S., Zomorrodi, R., Ghazala, Z., Cheam, A.S.M., Barr, M.S., Daskalakis, Z.J., Blumberger, D.M., Fischer, C., Flint, A., Mah, L., Herrmann, N., Bowie, C.R., Mulsant, B.H., Rajji, T.K., 2018. Theta-gamma coupling and working memory in Alzheimer's dementia and mild cognitive impairment. Front. Aging Neurosci. 10. doi:10.3389/fnagi.2018.00101.

Guo, Y., Hastie, T., Tibshirani, R., 2007. Regularized linear discriminant analysis and its application in microarrays. Biostatistics 8, 86–100. doi:10.1093/biostatistics/kxj035.

Haegens, S., Nácher, V., Luna, R., Romo, R., Jensen, O., 2011. α-Oscillations in the monkey sensorimotor network influence discrimination performance by rhythmical inhibition of neuronal spiking. Proc. Natl Acad. Sci. 108, 19377–19382. doi:10.1073/pnas.1117190108.

Hammer, J., Fischer, J., Ruescher, J., Schulze-Bonhage, A., Aertsen, A., Ball, T., 2013. The role of ECoG magnitude and phase in decoding position, velocity, and acceleration during continuous motor behavior. Front. Neurosci. 7. doi:10.3389/fnins.2013.00200.

Hammer, J., Pistohl, T., Fischer, J., Kršek, P., Tomášek, M., Marusič, P., Schulze-Bonhage, A., Aertsen, A., Ball, T., 2016. Predominance of movement speed over direction in neuronal population signals of motor cortex: intracranial EEG data and a simple explanatory model. Cereb Cortex 26, 2863–2881. doi:10.1093/cercor/bhw033.

Hemptinne, C.de, Ryapolova-Webb, E.S., Air, E.L., Garcia, P.A., Miller, K.J., Ojemann, J.G., Ostrem, J.L., Galifianakis, N.B., Starr, P.A., 2013. Exaggerated phase–amplitude coupling in the primary motor cortex in Parkinson disease. Proc. Natl Acad. Sci. 110, 4780–4785. doi:10.1073/pnas.1214546110.

Huang, N.E., Shen, Z., Long, S.R., Wu, M.C., Shih, H.H., Zheng, Q., Yen, N.-C., Tung, C.C., Liu, H.H., 1998. The empirical mode decomposition and the Hilbert spectrum for nonlinear and non-stationary time series analysis. Proc. Royal Soc. London. Series A 454, 903–995. doi:10.1098/rspa.1998.0193.

Hülsemann, M.J., Naumann, E., Rasch, B., 2019. Quantification of phase-amplitude coupling in neuronal oscillations: comparison of phase-locking value, mean vector length,

modulation index, and generalized-linear-modeling-cross-frequency-coupling. Front. Neurosci. 13. doi:10.3389/fnins.2019.00573.

Jenkinson, N., Kühn, A.A., Brown, P., 2013. Gamma oscillations in the human basal ganglia. Exper. Neurol. Special Issue 245, 72–76. doi:10.1016/j.expneurol.2012.07.005.

Jerbi, K., Vidal, J.R., Mattout, J., Maby, E., Lecaignard, F., Ossandon, T., Hamamé, C.M., Dalal, S.S., Bouet, R., Lachaux, J.-P., Leahy, R.M., Baillet, S., Garnero, L., Delpuech, C., Bertrand, O., 2011. Inferring hand movement kinematics from MEG, EEG and intracranial EEG: From brain-machine interfaces to motor rehabilitation. IRBM, NUMÉRO SPÉCIAL 32, 8–18. doi:10.1016/j.irbm.2010.12.004.

Kim, M.G., 2000. Multivariate outliers and decompositions of mahalanobis distance. Commun. Stat. Theor. Methods 29, 1511–1526. doi:10.1080/03610920008832559.

Klimesch, W., 1999. EEG alpha and theta oscillations reflect cognitive and memory performance: a review and analysis. Brain Res. Rev. 29, 169–195. doi:10.1016/S0165-0173(98)00056-3.

Knyazev, G.G., 2012. EEG delta oscillations as a correlate of basic homeostatic and motivational processes. Neurosci. Biobehav. Rev. 36, 677–695. doi:10.1016/j.neubiorev.2011.10.002.

Kondylis, E.D., Randazzo, M.J., Alhourani, A., Lipski, W.J., Wozny, T.A., Pandya, Y., Ghuman, A.S., Turner, R.S., Crammond, D.J., Richardson, R.M., 2016. Movement-related dynamics of cortical oscillations in Parkinson's disease and essential tremor. Brain 139, 2211–2223. doi:10.1093/brain/aww144.

Kramer, M.A., Tort, A.B.L., Kopell, N.J., 2008. Sharp edge artifacts and spurious coupling in EEG frequency comodulation measures. J. Neurosci. Methods 170, 352–357. doi:10.1016/j.jneumeth.2008.01.020.

Lalo, E., Thobois, S., Sharott, A., Polo, G., Mertens, P., Pogosyan, A., Brown, P., 2008. Patterns of bidirectional communication between cortex and basal ganglia during movement in patients with parkinson disease. J. Neurosci. 28, 3008–3016. doi:10.1523/JNEUROSCI.5295-07.2008.

Lawhern, V.J., Solon, A.J., Waytowich, N.R., Gordon, S.M., Hung, C.P., Lance, B.J., 2018. EEGNet: a compact convolutional neural network for EEG-based brain–computer interfaces. J. Neural Eng. 15, 056013. doi:10.1088/1741-2552/aace8c.

Leeb, R., Lee, F., Keinrath, C., Scherer, R., Bischof, H., Pfurtscheller, G., 2007. Brain–computer communication: motivation, aim, and impact of exploring a virtual apartment. IEEE Trans. Neural Syst. Rehabil. Eng. 15, 473–482. doi:10.1109/TNSRE.2007.906956.

López-Azcárate, J., Nicolás, M.J., Cordon, I., Alegre, M., Artieda, J., Valencia, M., 2013. Delta-mediated cross-frequency coupling organizes oscillatory activity across the rat cortico-basal ganglia network. Front. Neural Circuits 7. doi:10.3389/fncir.2013.00155.

Lozano-Soldevilla, D., ter Huurne, N., Oostenveld, R., 2016. Neuronal oscillations with non-sinusoidal morphology produce spurious phase-to-amplitude coupling and directionality. Front. Comput. Neurosci. 10. doi:10.3389/fncom.2016.00087.

Lutz, A., Greischar, L.L., Rawlings, N.B., Ricard, M., Davidson, R.J., 2004. Long-term meditators self-induce high-amplitude gamma synchrony during mental practice. Proc. Natl Acad. Sci. 101, 16369–16373. doi:10.1073/pnas.0407401101.

Maeder, C.L., Sannelli, C., Haufe, S., Blankertz, B., 2012. Pre-stimulus sensorimotor rhythms influence brain–computer interface classification performance. IEEE Trans. Neural Syst. Rehabil. Eng. 20, 653–662. doi:10.1109/TNSRE.2012.2205707.

Mahmood, A., Zainab, R., Ahmad, R.B., Saeed, M., Kamboh, A.M., 2017. Classification of multi-class motor imagery EEG using four band common spatial pattern. In: 2017 39th Annual International Conference of the IEEE Engineering in Medicine and Biology Society (EMBC). Presented at the 2017 39th Annual International Conference of the IEEE Engineering in Medicine and Biology Society (EMBC), pp. 1034–1037. doi:10.1109/EMBC.2017.8037003.

Malekmohammadi, M., AuYong, N., Ricks-Oddie, J., Bordelon, Y., Pouratian, N., 2018. Pallidal deep brain stimulation modulates excessive cortical high β phase amplitude coupling in Parkinson disease. Brain Stimul. 11, 607–617. doi:10.1016/j.brs.2018.01.028.

Maris, E., van Vugt, M., Kahana, M., 2011. Spatially distributed patterns of oscillatory coupling between high-frequency amplitudes and low-frequency phases in human iEEG. Neuroimage 54, 836–850. doi:10.1016/j.neuroimage.2010.09.029.

Meij, R.van der, Kahana, M., Maris, E., 2012. Phase–amplitude coupling in human electrocorticography is spatially distributed and phase diverse. J. Neurosci. 32, 111–123. doi:10.1523/JNEUROSCI.4816-11.2012.

Milekovic, T., Fischer, J., Pistohl, T., Ruescher, J., Schulze-Bonhage, A., Aertsen, A., Rickert, J., Ball, T., Mehring, C., 2012. An online brain–machine interface using decoding of movement direction from the human electrocorticogram. J. Neural Eng. 9, 046003. doi:10.1088/1741-2560/9/4/046003.

Miller, K.J., Hermes, D., Honey, C.J., Hebb, A.O., Ramsey, N.F., Knight, R.T., Ojemann, J.G., Fetz, E.E., 2012. Human motor cortical activity is selectively phase-entrained on underlying rhythms. PLoS Comput. Biol. 8, e1002655. doi:10.1371/journal.pcbi.1002655.

Mtui, E., Gruener, G., Dockery, P., 2020. Fitzgerald's Clinical Neuroanatomy and Neuroscience E-Book. Elsevier Health Sciences.

Munia, T.T.K., Aviyente, S., 2019. Time-frequency based phase-amplitude coupling measure for neuronal oscillations. Sci. Rep. 9, 12441. doi:10.1038/s41598-019-48870-2.

Muthukumaraswamy, S.D., Singh, K.D., 2011. A cautionary note on the interpretation of phase-locking estimates with concurrent changes in power. Clin. neurophysiol 122, 2324–2325.

Nam, C.S., Jeon, Y., Kim, Y.-J., Lee, I., Park, K., 2011. Movement imagery-related lateralization of event-related (de)synchronization (ERD/ERS): motor-imagery duration effects. Clin. Neurophysiol. 122, 567–577. doi:10.1016/j.clinph.2010.08.002.

Penny, W.D., Duzel, E., Miller, K.J., Ojemann, J.G., 2008. Testing for nested oscillation. J. Neurosci. Methods 174, 50–61. doi:10.1016/j.jneumeth.2008.06.035.

Pfurtscheller, G., Lopes da Silva, F.H., 1999. Event-related EEG/MEG synchronization and desynchronization: basic principles. Clin. Neurophysiol. 110, 1842–1857. doi:10.1016/S1388-2457(99)00141-8.

Pfurtscheller, G., Neuper, C., 1997. Motor imagery activates primary sensorimotor area in humans. Neurosci. Lett. 239, 65–68. doi:10.1016/S0304-3940(97)00889-6.

Pfurtscheller, G., Stancák, A., Neuper, C., 1996. Post-movement beta synchronization. A correlate of an idling motor area? Electroencephalogr. Clin. Neurophysiol. 98, 281–293. doi:10.1016/0013-4694(95)00258-8.

Pittman-Polletta, B., Hsieh, W.-H., Kaur, S., Lo, M.-T., Hu, K., 2014. Detecting phase-amplitude coupling with high frequency resolution using adaptive decompositions. J. Neurosci. Methods 226, 15–32. doi:10.1016/j.jneumeth.2014.01.006.

Porro, C.A., Cettolo, V., Francescato, M.P., Baraldi, P., 2000. Ipsilateral involvement of primary motor cortex during motor imagery. Eur. J. Neurosci. 12, 3059–3063. doi:10.1046/j.1460-9568.2000.00182.x.

Qiu, W., Kuang, H., Teleg, E., Ospel, J.M., Sohn, S.I., Almekhlafi, M., Goyal, M., Hill, M.D., Demchuk, A.M., Menon, B.K., 2020. Machine learning for detecting early infarction in acute stroke with non–contrast-enhanced CT. Radiology 294, 638–644. doi:10.1148/radiol.2020191193.

Schoffelen, J.-M., Oostenveld, R., Fries, P., 2005. Neuronal coherence as a mechanism of effective corticospinal interaction. Science 308, 111–113. doi:10.1126/science.1107027.

Schwertman, N.C., de Silva, R., 2007. Identifying outliers with sequential fences. Comput. Stat. Data Anal. 51, 3800–3810. doi:10.1016/j.csda.2006.01.019.

Wu, Shang-Lin, Wu, Chun-Wei, Pal, N.R., Chen, Chih-Yu, Chen, Shi-An, Lin, Chin-Teng, 2013. Common spatial pattern and linear discriminant analysis for motor imagery classification. In: 2013 IEEE Symposium on Computational Intelligence, Cognitive Algorithms, Mind, and Brain (CCMB). Presented at the 2013 IEEE Symposium on Computational Intelligence, Cognitive Algorithms, Mind, and Brain (CCMB), pp. 146–151. doi:10.1109/CCMB.2013.6609178.

Stevenson, N.J., Clancy, R.R., Vanhatalo, S., Rosén, I., Rennie, J.M., Boylan, G.B., 2015. Interobserver agreement for neonatal seizure detection using multichannel EEG. Ann. Clin. Transl. Neurol. 2, 1002–1011. doi:10.1002/acn3.249.

Suffczynski, P., 1999. Event-related dynamics of alpha band rhythms : a neuronal network model of focal ERD/surround ERS. Event-Related Desynchr. 6, 67–85.

Thomas, K.P., Guan, C., Lau, C.T., Vinod, A.P., Ang, K.K., 2009. A new discriminative common spatial pattern method for motor imagery brain–computer interfaces. IEEE Trans. Biomed. Eng. 56, 2730–2733. doi:10.1109/TBME.2009.2026181.

Tort, A.B.L., Komorowski, R., Eichenbaum, H., Kopell, N., 2010. Measuring phase-amplitude coupling between neuronal oscillations of different frequencies. J. Neurophysiol. 104, 1195–1210. doi:10.1152/jn.00106.2010.

Tort, A.B.L., Kramer, M.A., Thorn, C., Gibson, D.J., Kubota, Y., Graybiel, A.M., Kopell, N.J., 2008. Dynamic cross-frequency couplings of local field potential oscillations in rat striatum and hippocampus during performance of a T-maze task. Proc. Natl Acad. Sci. 105, 20517–20522. doi:10.1073/pnas.0810524105.

Tsai, F.-F., Fan, S.-Z., Cheng, H.-L., Yeh, J.-R., 2019. Multi-timescale phase-amplitude couplings in transitions of anesthetic-induced unconsciousness. Sci. Rep. 9, 7815. doi:10.1038/s41598-019-44238-8.

van Wijk, B.C.M., Jha, A., Penny, W., Litvak, V., 2015. Parametric estimation of cross-frequency coupling. J. Neurosci. Methods 243, 94–102. doi:10.1016/j.jneumeth.2015.01.032.

Voytek, B., Canolty, R.T., Shestyuk, A., Crone, N., Parvizi, J., Knight, R.T., 2010. Shifts in gamma phase–amplitude coupling frequency from theta to alpha over posterior cortex during visual tasks. Front. Hum. Neurosci. 4. doi:10.3389/fnhum.2010.00191.

Voytek, B., D'Esposito, M., Crone, N., Knight, R.T., 2013. A method for event-related phase/amplitude coupling. Neuroimage 64, 416–424. doi:10.1016/j.neuroimage.2012.09.023.

Waldert, S., Pistohl, T., Braun, C., Ball, T., Aertsen, A., Mehring, C., 2009. A review on directional information in neural signals for brain-machine interfaces. J. Physiol.-Paris, Neurorobotics 103, 244–254. doi:10.1016/j.jphysparis.2009.08.007.

Wang, Y., Gao, S., Gao, X., 2005. Common spatial pattern method for channel selection in motor imagery based brain-computer interface. In: 2005 IEEE Engineering in Medicine and Biology 27th Annual Conference. Presented at the 2005 IEEE Engineering in Medicine and Biology 27th Annual Conference, pp. 5392–5395. doi:10.1109/IEMBS.2005.1615701.

Whittingstall, K., Logothetis, N.K., 2009. Frequency-band coupling in surface EEG reflects spiking activity in monkey visual cortex. Neuron 64, 281–289. doi:10.1016/j.neuron.2009.08.016.

Wilkins, K.B., Yao, J., 2020. Coordination of multiple joints increases bilateral connectivity with ipsilateral sensorimotor cortices. Neuroimage 207, 116344. doi:10.1016/j.neuroimage.2019.116344.

Yanagisawa, T., Yamashita, O., Hirata, M., Kishima, H., Saitoh, Y., Goto, T., Yoshimine, T., Kamitani, Y., 2012. Regulation of motor representation by phase–amplitude coupling in the sensorimotor cortex. J. Neurosci. 32, 15467–15475. doi:10.1523/JNEUROSCI.2929-12.2012.

Yang, A.I., Vanegas, N., Lungu, C., Zaghloul, K.A., 2014. Beta-coupled high-frequency activity and beta-locked neuronal spiking in the subthalamic nucleus of Parkinson's disease. J. Neurosci. 34, 12816–12827. doi:10.1523/JNEUROSCI.1895-14.2014.

Yeh, C.-H., Shi, W., 2018. Identifying phase-amplitude coupling in cyclic alternating pattern using masking signals. Sci. Rep. 8, 2649. doi:10.1038/s41598-018-21013-9.

Yuan, H., Liu, T., Szarkowski, R., Rios, C., Ashe, J., He, B., 2010. Negative covariation between task-related responses in alpha/beta-band activity and BOLD in human sensorimotor cortex: An EEG and fMRI study of motor imagery and movements. Neuroimage 49, 2596–2606. doi:10.1016/j.neuroimage.2009.10.028.

Zhang, D.-X., Wu, X.-P., Guo, X., 2008. The EEG signal preprocessing based on empirical mode decomposition. In: 2008 2nd International Conference on Bioinformatics and Biomedical Engineering. Presented at the 2008 2nd International Conference on Bioinformatics and Biomedical Engineering, pp. 2131–2134. doi:10.1109/ICBBE.2008.862.